Master Thesis

Exciton environmental effect of single wall carbon nanotubes

Graduate School of Science, Tohoku University
Department of Physics

Ahmad Ridwan Tresna Nugraha

2010

Acknowledgements

I would like to use this opportunity to thank many people who contributed to this thesis over two years of my master course studies at Tohoku University. First of all, I am very indebted to my supervisor Professor Riichiro Saito for his teaching me the fundamentals of research, basic ideas in carbon nanotube physics, and also scientist attitudes. I really appreciate his patience with my slow writing rate and sometimes my "crazy" direction in research. I would like to thank Professor Yoshio Kuramoto, Professor Toshihiro Kawakatsu, Professor Yoshiro Hirayama, and Professor Katsumi Tanigaki for being my thesis examiners. I would like to express my gratitude to Dr. Kentaro Sato for teaching me the exciton program developed by him and our past group member Dr. Jie Jiang. Indirectly, I am also really helped by Dr. Georgii Samsonidze's tube libraries that have been shared in our group. My sincere thanks go to Mrs. Setsuko Sumino and Wako Yoko for helping out with numerous administrative matters. I am thankful to our MIT (Professor Mildred S. Dresselhaus and Professor Gene Dresselhaus) and Brazilian collaborators (Professor Ado Jorio and Paulo T. Araujo) who have helped me a lot when I wrote my first scientific paper submitted to Applied Physics Letters. I acknowledge Professor Yutaka Ohno and Professor Shigeo Maruyama for a fruitful discussion regarding the environmental effect. I am grateful to the former and present group members including Masaru Furukawa who was a very kind tutor for my first year life in Japan, Takahiro Eguchi, Dr. Li-Chang Yin, Rihei Endo, Md. Mahbubul Haque, and Mohammed Tareque Chowdhury for playing nice pingpong games. I thank Dr. Jin-Sung Park and Dr. Wataru Izumida who have been motivating me to do good research. I acknowledge a financial support from the MEXT scholarship. I am thankful to many other people who contributed to this thesis in one form or another. Last but not least, I dedicate this thesis to my family, especially my wife, whose time has been spent just for supporting me.

Contents

Chapter 1

Introduction

Carbon nanotubes (CNTs) are thin and hollow cylinders made out of entirely carbon atoms. These were discovered in the form of multi wall carbon nanotubes (MWNT) and single wall carbon nanotubes (SWNT) in 1991 and 1993, consecutively [1, 2]. SWNTs have a cylindrical shape of various lengths and diameters on the order of $1\,\mu$m and 1 nm, respectively. The diameter is small enough compared to the length, thus SWNT is regarded as a quasi one dimensional (1D) material. The structure of a SWNT can be conceptualized by wrapping a one-atom-thick layer of graphite (called graphene) into a seamless cylinder. The way the graphene sheet is rolled up is represented by a pair of integer index (n, m) called the chiral vector, which also gives both the nanotube diameter (d_t) and chiral angle (θ). Depending on the (n, m) value, the SWNTs can be either metallic or semiconducting. It has been predicted that one of three SWNTs shows metallic behavior, while the other two show semiconducting behavior [3]. These special electronic properties, which are not found in any other material, suggest many potential applications of SWNTs such as logical circuits, metallic wires, nanotube transistors, and optical devices [4, 5].

Optical spectroscopy methods, such as resonance Raman spectroscopy (RRS) and band gap photoluminescence (PL), have been proved to provide powerful tools for investigating the geometry and optical properties of SWNTs in different samples. They can be used to characterize electronic transitions between van Hove singularities (VHSs) in the density of states (DOS), which originate from the 1D structure of SWNTs. The transition energies E_{ii} between VHSs for SWNTs of different (n, m) indices are often mapped on the so-called Kataura plot [6, 7], that is widely used the in RRS and PL studies of SWNTs. The Kataura plot gives E_{ii} as a function of the tube diameter (d_t) or inverse diameter ($1/d_t$). The E_{ii} energies in the Kataura plot are arranged in bands ($E_{11}^{\mathrm{S}}, E_{22}^{\mathrm{S}}, E_{11}^{\mathrm{M}}$, etc.) for semiconducting (S) and metallic (M) SWNTs, where the index i denotes the transition between the ith VHS in the valence band to the ith VHS in the conduction band (i is counted from the Fermi level).

Early on, some aspects of the optical measurements of E_{ii} could be interpreted within the context of a simple noninteracting electron model [7, 8]. However, it has been clear that electron-electron and electron-hole interactions play an important role in determining the optical transition energies. Theoretical calculations and experimental measurements also showed that the exciton binding energies are very large in the nanotube system, up to 1 eV, indicating the importance of many-body effects in this quasi 1D system [9, 10, 11, **?**, 12, 13, 14, 15]. Thus, E_{ii} is now well understood in terms of excitonic transition energy (or simply exciton energy).

1.1 Purpose of the study

It has been found that E_{ii} is strongly influenced by a change in the surrounding materials, through the so-called environmental effect [16]. To accurately assign an (n, m) index, it is necessary to know very well E_{ii} (from the RRS or PL measurements) and radial breathing mode (RBM) frequencies measured from the RRS experiments for a standard SWNT and how environmental effects can change such standard properties. While the RBM frequency behavior when the tube is interacting with some environments has been mostly understood by some empirical formulas [17, **?**], a complete description for the E_{ii}'s environmental effect

is still missing. Theoretical calculations which take into account curvature and many-body effects are still insufficient to accurately describe the experimentally obtained E_{ii} results. The reason is that E_{ii} strongly depends on the dielectric constant of the SWNT and its environment [18]. Consequently, lots of different values of E_{ii} published in the literature are urging the need for one big unified picture.

In this thesis, we are going to discuss some main aspects of finding an appropriate description for the SWNT's environmental dielectric screening effect within exciton picture, therefore describe all E_{ii} values. In short, the purpose of the present study is as follows.

- To model the environmental effect on E_{ii} in terms of the excitonic dielectric screening effect.
- To find a formula for reproducing experimentally obtained E_{ii} for many SWNT chiralities in different samples, hence providing an accurate assignment of (n, m) indices and establishing a standard reference for SWNT characterization from the theoretical point of view.

1.2 Background

1.2.1 Nanotube synthesis

The synthesis of CNTs is an important issue in the nanotube research field since it determines many aspects of the physical properties of the CNTs. Chirality control is particularly the most difficult part to achieve, no one has yet given a nanotube of single (n, m) index. Nevertheless, some techniques have been developed to produce nanotubes in sizeable quantities, such as arc discharge, laser ablation, and chemical vapor deposition (CVD). Such processes in the nanotube synthesis, along with the surfactants used to disperse or isolate SWNTs, play a significant role in the environmental effects. Most of these processes take place in vacuum or with additional gases and thus have special characteristics related to their dielectric properties. Here we review some of these synthesis methods.

Arc discharge

Nanotubes were observed in 1991 in the carbon soot of graphite electrodes during an arc discharge by using a high current, that was intended to produce fullerenes [1]. The first macroscopic production of CNTs was made in 1992 at NEC Fundamental Research Laboratory [19]. During this process, the carbon contained in the negative electrode sublimates because of the high discharge temperatures. This method produces both SWNTs and MWNTs with lengths of up to 50 μm and only few structural defects.

Laser ablation

In the laser ablation process, a pulsed laser vaporizes a graphite target in a high-temperature reactor while an inert gas is blowed into the reaction chamber. Nanotubes grow on the cooler surfaces of the reactor as the vaporized carbon condenses. To collect the nanotubes, a water-cooled surface can be included in the system. This process was developed by R. Smalley and co-workers at Rice University. Actually at the time of the discovery of CNTs, they were only blasting metals with a laser to produce various metal molecules. When they realized the possibility of making nanotubes, they then replaced the metals with graphite to create MWNTs. Later on, they used a composite of graphite and metal catalyst particles to synthesize SWNTs [20, 21]. This method produces mainly SWNTs with a controllable diameter that can be determined by the reaction temperature.

Chemical vapor deposition (CVD)

CNTs were first successfully formed by this process in 1993 [22]. During the deposition, a substrate is prepared with a layer of metal catalyst particles, such as nickel, cobalt, iron, or a combination. The diameters of the nanotubes to be grown are related to the size of the metal catalysts. This can be controlled by patterned deposition of the metal, annealing, or by plasma etching of a metal layer. The substrate is then heated up to approximately 700°C. To induce the growth of the nanotubes, two kinds of gases are bled into the reactor. The first one is a process gas such as ammonia, nitrogen or hydrogen and the second one is

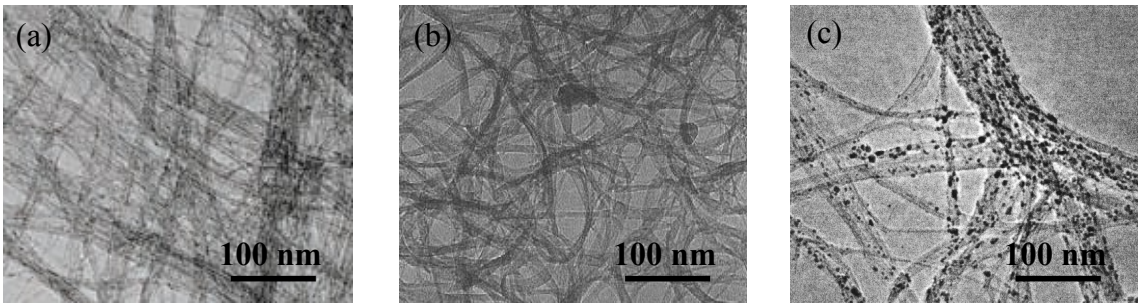

Figure 1-1: TEM image of SWNTs produced by three CVD methods. (a) Super-growth: Water-assisted CVD results in massive growth of superdense aligned nanotube forests [**?**]. (b) ACCVD: High purity SWNTs synthesized at low temperature by using alcohol as the carbon source [23]. (c) HiPco: Catalytic production of SWNTs in a continuous-flow gas-phase process using carbon monoxide as the carbon feedstock [24].

carbon-containing gas such as acetylene, ethylene, ethanol or methane. Nanotubes grow at the sites of the metal catalyst, then the carbon-containing gas is broken apart at the surface of the catalyst particle, and the carbon is transported to the edges of the particle, where it forms the nanotubes.

Of the various methods for synthesizing nanotubes, CVD is the most promising process for industrial-scale production because of its price per unit ratio, small defects, and it is also capable of growing nanotubes directly on a desired substrate, whereas in the other growth techniques the nanotubes must be collected individually. There are several well-known variations of the CVD method. Three of which are water-assisted CVD or the so-called super-growth method (SG) [**?**], alcohol-catalytic CVD (ACCVD) [23], and high pressure carbon monoxide decomposition (HiPco) [24]. They provide SWNTs of high-quality within a broad range of diameters in different environments, thus suit the needs of E_{ii} analysis in this thesis.

In the HiPco process, catalysts for SWNT growth form *in situ* by thermal decomposition of iron pentacarbonyl in a heated flow of carbon monoxide at pressures of $1 - 10$ atm and temperatures of $800 - 1200°$C. The SWNT yield and diameter distribution can be varied by controlling the process parameters, and SWNTs as small as 0.7 nm in diameter (the same as

Fig. 1-1: fig/fch1-cnt.pdf

that of a C_{60} molecule) have been generated. Usually the SWNTs produced by the HiPco method is further dispersed in the sodium docedyl sulfate (SDS) solution.

In the ACCVD process, alcohol is used as the carbon source and high-purity SWNTs can be grown at relatively low temperature. Because of the etching effect of decomposed OH radical attacking carbon atoms with a dangling bond, impurities such as amorphous carbon, multi wall carbon nanotubes, metal particles and carbon nanoparticles are completely suppressed even at reaction temperature as low as $700 - 800°C$. By using methanol, generation of SWNTs even at 550°C can be achieved.

In the SG method, the activity and lifetime of the catalyst are enhanced by addition of water into the CVD reactor. Dense millimeter-tall nanotube "forests", aligned normal to the substrate, are produced. Those SWNT forests can be easily separated from the catalyst, yielding clean SWNT material (purity $> 99.98\,\%$) without further purification, and thus the surrounding materials around the SWNTs are almost like vacuum. For comparison, the as-grown HiPco CNTs contain about $5 - 35\,\%$ of metal impurities. It is therefore purified through dispersion (such as by SDS) and centrifugation that damages the nanotubes. The SG process allows to avoid this problem. It is also possible to grow material containing SWNT, DWNTs and MWNTs, and to alter their ratios by tuning the growth conditions, thus the SG method generally provides a very broad distribution of the nanotube diameter.

1.2.2 Measurements of optical transition energies

The optical transition energies E_{ii} of SWNTs are a key signature for the nanotube structure assignment. The E_{ii} measurements give rich information about the electronic structure of an SWNT, for example, whether the SWNT is metallic or semiconducting. Based on these measurements, the tube diameter d_t and chiral index (n, m) can also be determined. These are usually performed by using photoluminescence (PL) and resonance Raman spectroscopy (RRS).

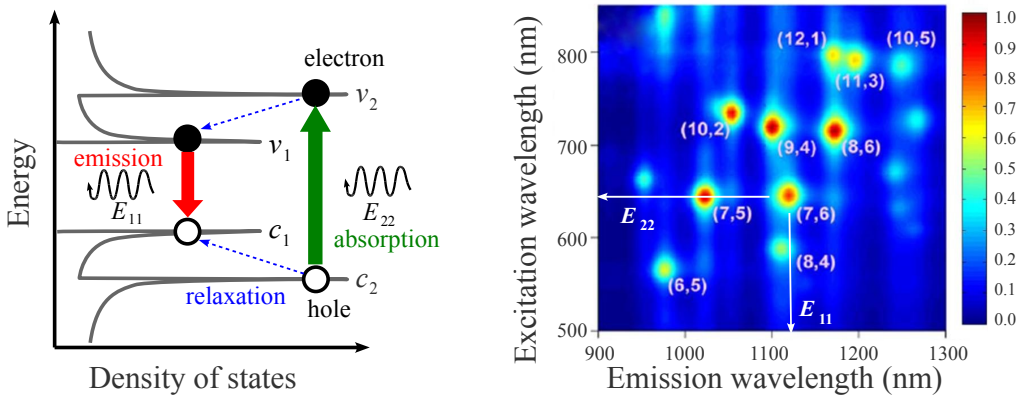

Figure 1-2: (a) Schematic density of electronic states (DOS) illustrating PL process. See text for details. (b) 2D PL intensity map giving some (n, m) values [25].

Photoluminescence spectroscopy

In PL spectroscopy, metallic SWNTs (M-SWNTs) do not fluoresce because they have no band gaps. In the case of semiconducting SWNTs (S-SWNTs), there is a direct energy gap so that a strong light absorption and emission can occur. Surfactant materials are used to separate S-SWNTs from M-SWNTs in a bundle of SWNTs, and then PL spectra can be observed for S-SWNTs.

The excitation of PL can be described as is illustrated in Fig. 1-2(a). An electron in a SWNT absorbs excitation light via E_{22} transition, creating an electron-hole pair. The electron and hole rapidly relax through phonon-assisted processes from c_2 (second conduction) to c_1 (first conduction) and from v_2 (second valence) to v_1 (first valence) states, respectively. They then recombine through c_1 to v_1 transition resulting in light emission (E_{11}). For M-SWNTs, an electron can actually be excited, thus resulting in optical absorption, but the hole is immediately filled by another electron out of many available in the metal. Therefore no electron-hole pair is produced and the light emission cannot be observed.

In Fig. 1-2(b) PL intensity is plotted versus excitation and emission wavelengths (of

Fig. 1-2: fig/fch1-pl.pdf

light) where we can see some strong peaks corresponding to a certain PL process. Since the DOS of each SWNT is unique, thus each strong peak should corresponds to a particular tube structure, that is one (n, m) value of S-SWNT. PL spectroscopy is therefore a very important tool for S-SWNT characterization.

Resonance Raman spectroscopy

Raman spectroscopy is basically understood as an inelastic light scattering process. The process is slightly different from the PL process. A given laser light can excite an electron from a conduction band to a valence band, leaving a hole in the valence band. The photo-excited electron goes down to a virtual state whose lifetime is very short by emitting phonon, then the electron recombines with hole resulting in the emitted light. Intensity of the emitted light is very weak; however, when the laser energy is resonant to the energy gap between the conduction and valence bands, the intensity is strongly enhanced, thus giving information of E_{ii}. This is called resonance Raman spectroscopy (RRS). Several scattering modes dominate the Raman spectrum, such as the radial breathing mode (RBM), D mode, G mode, and G' mode, which are all related to a special phonon energy. The phonon frequency involved in the Raman spectroscopy process is called Raman shift. An illustration of some phonon modes in a Raman spectrum is shown in Fig. 1-3(a).

For characterization purposes, the RBM is particularly of great importance since it is directly related to the nanotube diameter d_t [27]. The RBM corresponds to radial expansion and contraction of the tube. Its frequency, ω_{RBM}, depends on d_t and can be estimated by $\omega_{\mathrm{RBM}} = A/d_t + B$, where A and B are fitted for various nanotube samples [**?**]. This relation is very useful for extracting the nanotube diameter from the RBM position. A typical RBM range is about $100 - 350\,\mathrm{cm}^{-1}$. Similar to the PL map, the energy of the excitation light can be scanned in Raman measurements, thus producing a Raman excitation profile. Those maps also contain oval-shaped features uniquely identifying (n, m) indices. An example of such maps is shown in Fig. 1-3(b), where the RBM Raman intensity is plotted as a function

Fig. 1-3: fig/fch1-raman.pdf

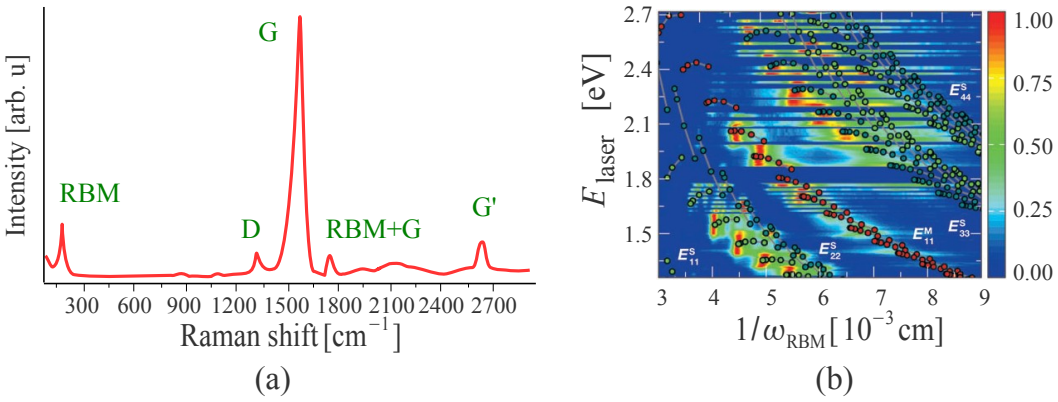

Figure 1-3: (a) Cartoon of a Raman spectrum of SWNTs for a given laser energy. (b) 2D Raman intensity map showing the SWNT RBM spectral evolution as a function of laser excitation energy [26]. Dots are 378 E_{ii} values of all SWNTs in the experimental range.

of laser excitation energy and RBM frequency. In contrast to PL, Raman spectroscopy can detect not only semiconducting but also metallic tubes, and it is less sensitive to nanotube bundling than PL. However, requirement of a tunable laser and a special spectrometer might be strong technical drawbacks.

1.2.3 Importance of exciton picture

Basically, an exciton consists of a photo-excited electron and a hole bound to each other by a Coulomb interaction in a semiconducting material. In most semiconductors, we can calculate the binding energy of an exciton in 3D materials by a hydrogenic model with a reduced effective mass and a dielectric constant. The resulting binding energy is on the order of 10 meV, thus optical absorption to exciton levels is usually observed only at low temperatures. However, in an SWNT, because of its 1D properties, the electron-hole attraction energy becomes larger and can be as large as 1 eV, so exciton effects can be observed at room temperature. Excitons are therefore essential for explaining optical processes in SWNTs.

In order to explain the observed E_{ii}, much insight has been gained from the simple

Fig. 1-4: fig/fch1-kata.pdf

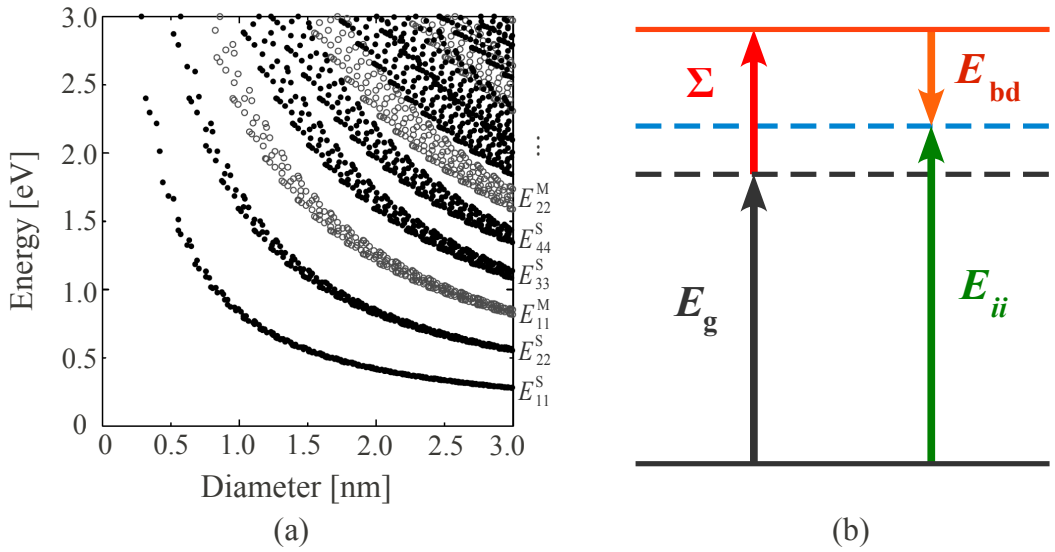

Figure 1-4: (a) STB Kataura plot, the vertical energy axis is the nanotube band gap [7]. (b) Single particle band gap E_g is not simply the transition energy. Self energy Σ and binding energy $E_{\rm bd}$ corrections give the true transition energy E_{ii}.

(nearest-neighbor) tight-binding (STB) model of the band structure of SWNTs [7]. This method predicts the transition energies varying approximately as the inverse of diameter and having a weak dependence on the chiral angle, as shown in the STB Kataura plot in Fig. 1-4(a). However, experimental and theoretical results point to the fact that the STB calculation is insufficient for an accurate description of optical transitions in SWNTs. For example, as has been reported by Weisman *et al.*, the E_{ii} values calculated by STB model are lower than those measured in their PL experiment [28]. They also observed the so-called family spread, in which nanotubes with the same $(2n + m)$ show a unique pattern for the smaller d_t.

The electron-electron and electron-hole interactions change in a significant way the E_{ii} dependence on diameter. Both the electron-electron and electron-hole interactions are due to screened Coulomb interactions. The former describes the repulsive energy, called self-energy Σ, that is needed to add an additional electron to the system, hence, increases the band gap. In contrast, the electron-hole interaction gives the attractive Coulomb interaction,

Fig. 1-5: fig/fch1-tp.pdf

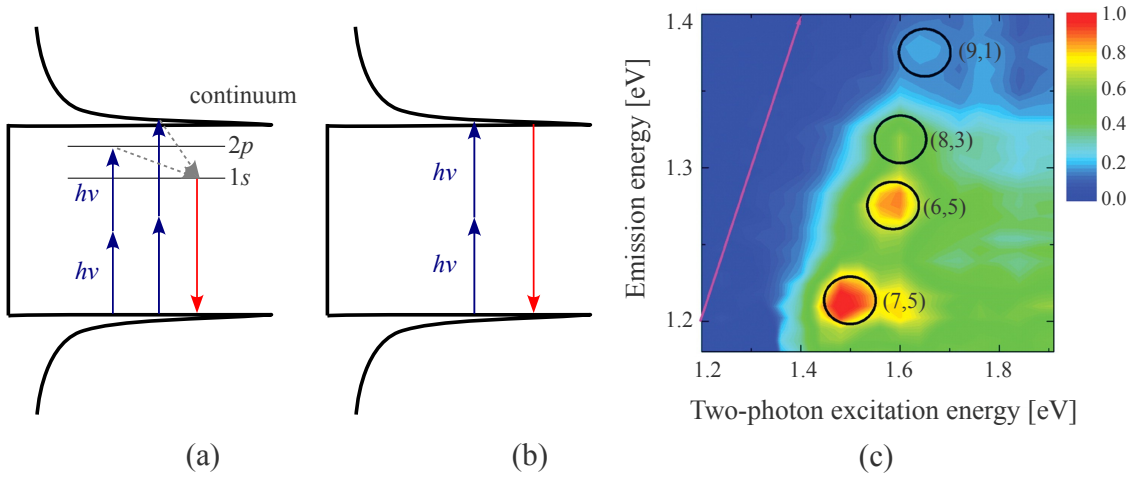

Figure 1-5: Two-photon experiment by Wang *et al.* [10]. (a) In the exciton picture, the $1s$ exciton state is forbidden under two-photon excitation. The $2p$ exciton and continuum states are excited. They relax to the $1s$ exciton state and fluoresce through a one-photon process. (b) In the simple band picture, two-photon excitation energy is the same as emission energy, but this case is not observed. (c). Contour plot of two-photon excitation spectra of SWNTs. By comparison with the solid line describing equal excitation and emission energies, it is clear that the two-photon excitation peaks are shifted above the energy of the corresponding emission feature. The large shift arises from the excitonic nature of SWNT optical transitions. $E_{\rm bd}$ is found to be as large as up to 1 eV, thus excitons play an important role in the nanotube optics.

called exciton binding energy $E_{\rm bd}$, which lowers the excitation energy. The overall effect is a blue-shift so that the positive self energy dominates over the negative exciton binding energy. This is illustrated in Fig. 1-4(b).

Experimentally, the importance of many-body effects in the form of excitonic electron-hole attraction and Coulombic electron-electron repulsion in SWNTs was discussed extensively for the first time in the context of the so-called ratio problem [29, 11], where the ratio between the second and first transition energies in S-SWNTs are not equal to two as predicted by the STB model [7]. Other experimental results, for example, the two-photon absorption experiments [10, **?**], then provided strong evidence for the excitonic nature of the lower energy transition. A two-photon experiment by Wang *et al.*, which is the first breakthrough in the nanotube $E_{\rm bd}$ measurements, is described in Fig. 1-5, after Ref. [10].

From the theoretical point of view, the importance of excitons was introduced very early by T. Ando who studied excitations of nanotubes within a static screened Hartree-Fock approximation [9]. After some experimental results started to show the rise of excitons, detailed first-principles calculations of the effects of many-body interactions on the optical properties of SWNTs were then performed [12, 13]. Some descriptions of excitons in nanotubes based on simpler or different models were also developed [14, 15]. In this thesis, however, the so-called extended tight-binding (ETB) model will be used to study the systematic dependence of exciton effects on the tube diameter and chiral angle [30]. In this model, the Bethe-Salpeter equation is solved for obtaining the excitation energies E_{ii} that already includes self energy and exciton binding energy. The ETB model also includes the curvature effects through the σ-π hybridization that cannot be neglected for nanotubes of small diameter.

1.2.4 Environmental effects

Optical absorption, photoluminescence, and resonance Raman spectroscopy have all been used to determine the E_{ii} energy values, leading to the development of theoretical models to describe the nanotube electronic structure for excited states. However, the E_{ii} values of a particular (n, m) SWNT have been found to shift by a large amount (up to 100 meV) by the effects of the substrate, bundling, and other environmental factors surrounding the SWNTs such as solvents or wrappings, and even temperature [16].

There are several experimental observations on these effects. Fig. 1-6(a) shows a PL measurement by Ohno *et al.* by changing surrounding materials around SWNTs. It is clearly shown the decrease of E_{ii} with increasing dielectric constant (or relative permittivity) of surrounding materials, κ_{env}. This indicates the exciton is screened more by higher dielectric constant materials, thus the energy decreases. In another experiment by Fantini *et al.* which is an early experiment on the environmental effects [16], they measured RRS E_{ii} values for some (n, m) nanotubes made by HiPco process and compared the results in bundles, those wrapped with sodium docedyl sulfate (SDS) in aquaeous solution, and also those wrapped

Fig. 1-6: fig/fch1-env.pdf

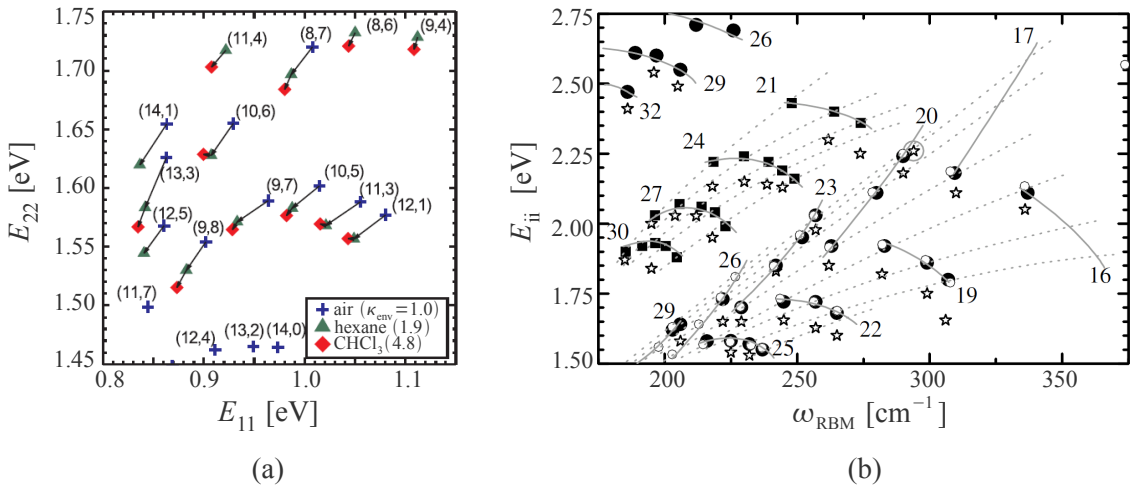

Figure 1-6: (a) PL measurement for three different surrounding materials around SWNTs with their own dielectric constants: air ($\kappa_{\rm env} = 1.0$), hexane ($\kappa_{\rm env} = 1.9$), and chloroform ($\kappa_{\rm env} = 4.8$). These substances are respectively denoted by plus, triangle, and diamond symbols. (b) Experimental E_{ii} versus $\omega_{\rm RBM}$ for 46 different (n, m) carbon nanotubes measured by RRS. Solid circles and solid squares denote, respectively, semiconducting and metallic SWNTs wrapped with SDS in aqueous solution. Open stars are for SWNTs in bundles. Open circles are for SWNTs wrapped in SDS measured by PL spectroscopy [28].

in SDS measured by PL spectroscopy [28]. Two main conclusions are obtained from their observation. First, for a given nanotube, the E_{ii} value is down-shifted for SWNT bundles compared to SWNTs in solution, as can be seen in 1-6(b). The shifts are different (from 20 up to 140 meV) for different (n, m) SWNTs. Second, the E_{ii} measurements by RRS and PL spectroscopy show good agreement to each other, thus it is quite safe to consider both the methods will give the same E_{ii} results, though in the later chapter it will be shown a necessary correction to the lowest transition energies in semiconducting SWNTs measured by PL spectroscopy. In a sense of the nanotube synthesis, the different synthesis methods may also give different E_{ii} for a certain (n, m) SWNT. The experimental E_{ii} values of SWNTs made by ACCVD and HiPco methods are generally red-shifted when compared to those made by SG method [31]. The Kataura plot becomes unique for each environment, and therefore the environmental effect must be taken into account explicitly.

Fig. 1-7: fig/fch4-sg1kapp.pdf

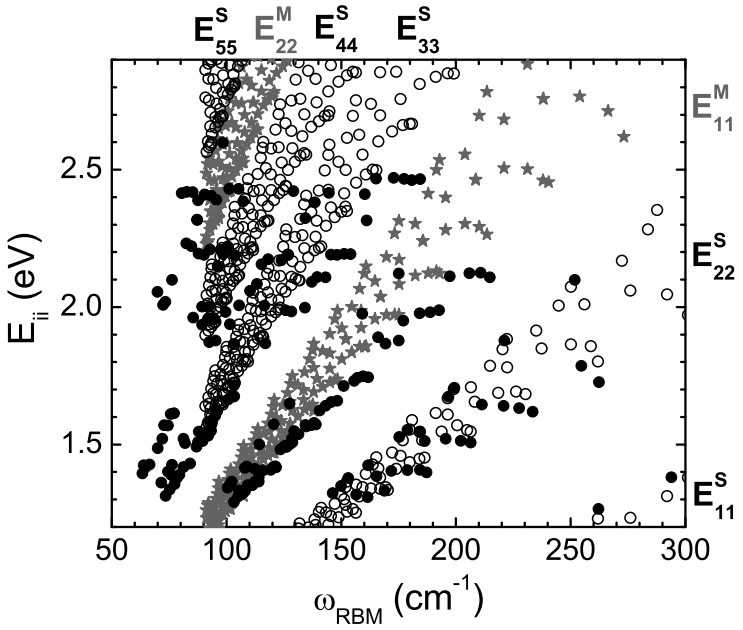

Figure 1-7: Black dots show $E_{ii}^{\rm exp}$ vs. $\omega_{\rm RBM}$ results from resonance Raman spectra taken for a SG sample [31, 32]. The black open circles (S-SWNTs) and the dark-gray stars (M-SWNTs) give $E_{ii}^{\rm cal}$ calculated with the smallest dielectric constant. Along the x axis, $E_{ii}^{\rm cal}$ are translated using the relation $\omega_{\rm RBM} = 227/d_t$ [17] which is valid for the SG sample.

Figure 1-7 shows a map of experimental E_{ii} values (black dots) [31, 32] from a SWNT sample grown by the "super-growth" (SG), water-assisted chemical CVD [**?**]. The resulting data for the E_{ii} transition energies are plotted as a function of the radial breathing mode frequencies $\omega_{\rm RBM}$ obtained by RRS. The experimental transition energy values $E_{ii}^{\rm exp}$ for the SG sample are compared with the calculated bright exciton energies $E_{ii}^{\rm cal}$ (open circles and stars), obtained for the smallest dielectric constant. Although $E_{ii}^{\rm cal}$ includes SWNT curvature and many-body effects, the $E_{ii}^{\rm exp}$ values are clearly redshifted when compared to the theory. More emphasis on this fact is shown in Fig. 1-8, in which the $E_{ii}^{\rm exp}$ values for the SG and ACCVD samples are compared. The $E_{ii}^{\rm exp}$ values for the ACCVD sample are red-shifted from those for the SG sample, thus they are also red-shifted from the theoretical results. Generally, this tendency is true for all experimental E_{ii} data available in the literature [31]. The redshift depends on both $\omega_{\rm RBM}$ (or on d_t) and the optical energy levels denoted by i in

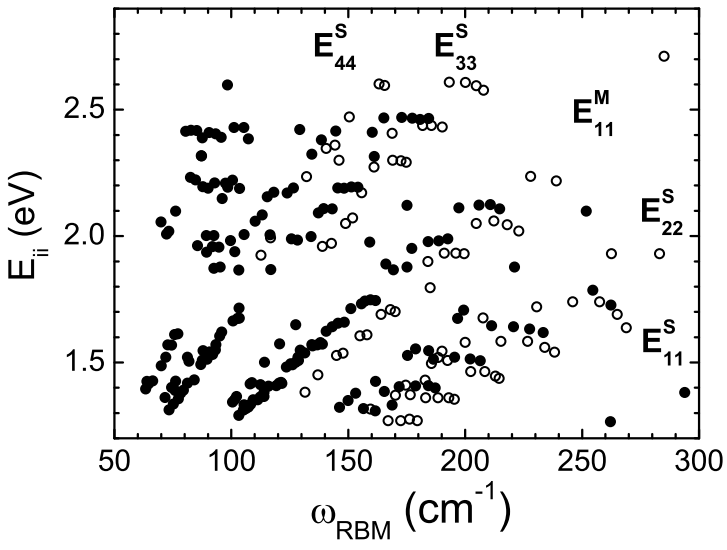

Figure 1-8: $E_{ii}^{\rm exp}$ vs. $\omega_{\rm RBM}$ experimental results obtained for the SG (bullets) and the ACCVD (open circles) SWNT samples.

E_{ii}.

The environmental effect on E_{ii} can be understood by the excitonic dielectric screening effect. Previous theoretical studies of E_{ii} mostly described the screening effect by a static dielectric constant κ which consists of screening terms by the surrounding materials ($\kappa_{\rm env}$) and the nanotube itself ($\kappa_{\rm tube}$). Calculations by Jiang *et al.* using a single constant $\kappa = 2.22$ provided a good description for the optical transition energies of bundled SWNTs for a limited range of d_t [30, 33]. In parallel, Miyauchi *et al.* used $1/\kappa = C_{\rm tube}/\kappa_{\rm tube} + C_{\rm env}/\kappa_{\rm env}$, where $C_{\rm tube}$ and $C_{\rm env}$ are d_t-dependent coefficients, and they successfully reproduced experimental E_{ii} values, though only for a very limited number of E_{11} transitions for S-SWNTs [18]. Other sophisticated theoretical models on this subject have also been presented [34, 35], but these formulations might be too complicated to be used for practical purposes.

Recently, Araujo *et al.* reported a d_t-dependent κ that could reproduce many experimental E_{ii} values and thus represents a breakthrough toward tackling the environmental

Fig. 1-8: fig/fch4-sgaa.pdf

effects [32]. However, different κ dependencies on d_t were obtained for $(E_{11}^{\mathrm{S}}, E_{22}^{\mathrm{S}}, E_{11}^{\mathrm{M}})$ relative to $(E_{33}^{\mathrm{S}}, E_{44}^{\mathrm{S}})$. In this thesis, it will be shown a significant improvement for the κ function which can unify all the dependencies for (E_{11}^{S}, E_{22}^{S}, E_{11}^{M}, E_{33}^{S}, E_{44}^{S}) over a broad range of d_t ($0.7 < d_t < 2.5\,\mathrm{nm}$). Now κ is found not only to depend on d_t, but also on the exciton size l_k in reciprocal space. An empirical formula to calculate unknown E_{ii} for different sample environments is then established.

1.3 Organization

This thesis is organized into five chapters. In Chapter 1, all the necessary backgrounds have been introduced. In Chapter 2, the basics of carbon nanotubes are reviewed, especially regarding the geometry and electronic structure. The electronic structure is considered within STB and ETB models. In Chapter 3, the calculation methods used in this thesis are discussed. The exciton energy calculation based on the ETB model is reviewed, which was developed by Jiang *et al.* [30] in our group. The main (original) results of this thesis will be shown in Chapter 4. The dependence of the exciton energy on the dielectric constant leads to the development of dielectric constant model which can reproduce many experimental E_{ii} values. A general functional form of κ is obtained, and it yields a parameter specific to each type of environments surrounding the nanotubes, therefore characterizes that environment. This function can then explain the environmental effect on the exciton energies. Furthermore, it can also be used to construct another empirical formula that relates E_{ii} directly to environmental dielectric constant and with a dependence on the nanotube diameter. Also, another important result from this work is that the super-growth SG sample can be considered as a standard for calculating E_{ii} values of other experimental samples. However, a small correction for E_{11}^{S} experimental data obtained by PL spectroscopy is needed. The reason is that there is a deviated tendency of the κ values for type-I and type-II S-SWNTs for E_{11}^{S} only. This deviation suggests that the exciton is thermally activated by the center of mass motions coupled with phonons. Finally, in Chapter 5, a summary of this thesis is given.

Chapter 2

Basics of carbon nanotubes

The basic properties of single wall carbon nanotubes (SWNTs) are reviewed in this chapter. The discussion includes a description of the nanotube geometrical structure and electronic properties. Because a SWNT can be imagined as a single layer graphene sheet rolled up into a cylinder, its electronic properties are inferred based on the electronic properties of graphene. Some important definitions related to the nanotube properties will be explained. The derivation of the electronic structure itself is within the tight-binding framework.

2.1 Geometrical structure

2.1.1 Graphene unit cell

Graphene is a single atomic layer of carbon atoms in a two-dimensional (2D) honeycomb lattice. Graphene is a basic building block for all graphitic materials of other dimensionalities. Several layers of graphene sheet stacked together will form 3D graphite, where the carbon atoms in each 2D layer make strong sp^2 bonds and the van der Waals forces describe a weak interlayer coupling. In 0D, graphene can be wrapped up into fullerenes, and in 1D, as a main discussion in this chapter, it can be rolled up to form the nanotubes.

Fig. 2-1: fig/fch2-grunit.pdf

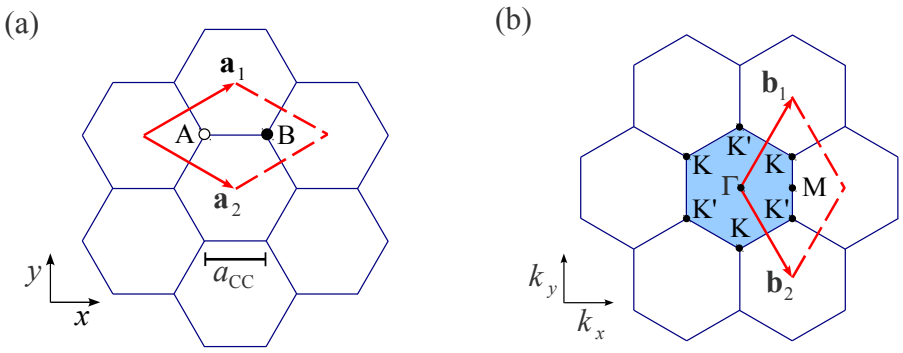

Figure 2-1: (a) The unit cell and (b) Brillouin zone of graphene are shown, respectively, as the dotted rhombus and the shaded hexagon. $\mathbf{a}_i$ and $\mathbf{b}_i$, where $i = 1, 2$, are unit vectors and reciprocal lattice vectors, respectively. The unit cell in real space contains two carbon atoms A and B. The dots labeled Γ, K, K′, and M in the Brillouin zone indicate the high-symmetry points.

Figure 2-1 gives the unit cell and Brillouin zone of graphene. The graphene sheet is generated from the dotted rhombus unit cell shown by the lattice vectors $\mathbf{a}_1$ and $\mathbf{a}_2$, which are defined as

$$\mathbf{a}_1 = a\left(\frac{\sqrt{3}}{2}, \frac{1}{2}\right), \quad \mathbf{a}_2 = a\left(\frac{\sqrt{3}}{2}, -\frac{1}{2}\right), \tag{2.1}$$

where $a = \sqrt{3}a_{CC}$ is the lattice constant for the graphene sheet and $a_{CC} \approx 0.142\,\text{nm}$ is the nearest-neighbor interatomic distance. The unit cell surrounds two distinct carbon atoms from the A and B sublattices shown, respectively, by open and solid dots in Fig. 2-1(a).

The reciprocal lattice vectors $\mathbf{b}_1$ and $\mathbf{b}_2$ are related to the real lattice vectors $\mathbf{a}_1$ and $\mathbf{a}_2$ according to the definition

$$\mathbf{a}_i \cdot \mathbf{b}_j = 2\pi\delta_{ij}, \tag{2.2}$$

where δ_{ij} is the Kronecker delta, so that $\mathbf{b}_1$ and $\mathbf{b}_2$ are given by

$$\mathbf{b}_2 = \frac{2\pi}{a}\left(\frac{1}{\sqrt{3}}, 1\right), \quad \mathbf{b}_2 = \frac{2\pi}{a}\left(\frac{1}{\sqrt{3}}, -1\right). \tag{2.3}$$

The first Brillouin zone is shown as a shaded hexagon in Fig. 2-1(b), where Γ, K, K′, and M denote the high symmetry points.

2.1.2 Nanotube unit cell

Carbon nanotube forms a periodical structure or lattice, which are non-bravais lattice since it is a 1D structure. Referring to the unrolled graphene sheet shown in Fig. 2-2, the unit cell of a SWNT is limited by two vectors: the chiral vector $\mathbf{C}_h$, and its pair, the translational vector $\mathbf{T}$. The chiral vector is defined as the way the graphene sheet is rolled up. It gives the circumference of the SWNT. One-dimensional periodicity is then determined by the vector perpendicular to the chiral vector, that is the translational vector.

The chiral vector $\mathbf{C}_h$ can be written in terms of the unit vectors of graphene $\mathbf{a}_1$ and $\mathbf{a}_2$,

$$\mathbf{C}_h = n\mathbf{a}_1 + m\mathbf{a}_2 \equiv (n, m), \tag{2.4}$$

where (n, m) is a pair of positive integer indices with $n \geq m$. Since $\mathbf{C}_h$ specifies the circumference of the SWNT, it is straightforward to obtain the relations for the circumferential length L and diameter d_t:

$$L = |\mathbf{C}_h| = a\sqrt{n^2 + nm + m^2}, \tag{2.5}$$

$$d_t = \frac{L}{\pi} = \frac{a\sqrt{n^2 + nm + m^2}}{\pi}. \tag{2.6}$$

The chiral angle θ is the angle between $\mathbf{C}_h$ and $\mathbf{a}_1$, with values of θ in the range of $0 \leq |\theta| \leq 30°$. Taking the inner product of $\mathbf{C}_h$ and $\mathbf{a}_1$, an expresion for $\cos\theta$ can be obtained, thus relating θ to the chiral index (n, m),

$$\cos\theta = \frac{\mathbf{C}_h \cdot \mathbf{a}_1}{|\mathbf{C}_h||\mathbf{a}_1|} = \frac{2n + m}{2\sqrt{n^2 + nm + m^2}}. \tag{2.7}$$

As can be seen in Fig. 2-2, the translation vector $\mathbf{T}$ is perpendicular to $\mathbf{C}_h$ and thus become the tube axis, it can be expressed as

$$\mathbf{T} = t_1\mathbf{a}_1 + t_2\mathbf{a}_2 \equiv (t_1, t_2), \tag{2.8}$$

Fig. 2-2: fig/fch2-construct.pdf

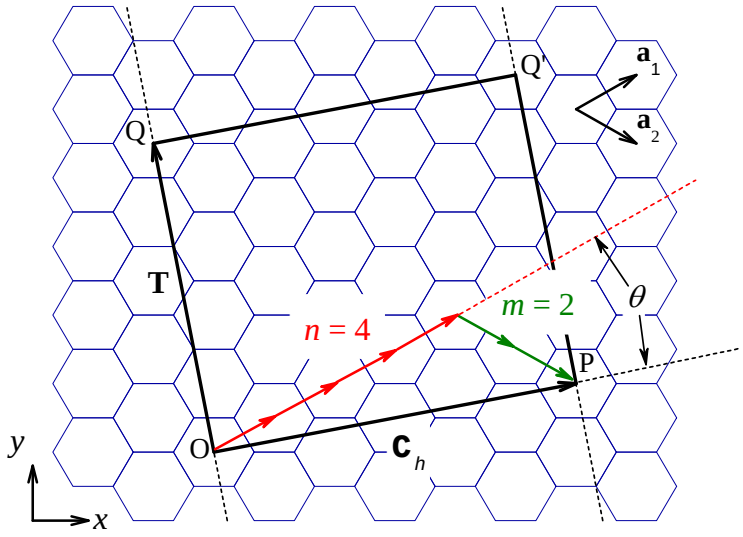

Figure 2-2: Geometry of a $(4, 2)$ SWNT viewed as an unrolled graphene sheet with the graphene unit vectors $\mathbf{a}_1$ and $\mathbf{a}_2$. The rectangle OPQ'Q is the 1D SWNT unit cell. Total hexagons covered within this rectangle unit cell is $N = 28$. **OP** and **OQ** define the chiral vector $\mathbf{C}_h$ and translation vector $\mathbf{T}$, respectively, whereas the chiral angle θ is the angle between $\mathbf{a}_1$ and $\mathbf{C}_h$. From the figure, it is obvious $\mathbf{C}_h = (4, 2)$ and $\mathbf{T} = (4, -5)$. If the site O is connected to P, and the site Q is connected to Q', the cylindrical SWNT can be constructed.

where t_1 and t_2 are obtained from the condition $\mathbf{C}_h \cdot \mathbf{T} = 0$,

$$t_1 \frac{2m + n}{d_R} \quad t_2 = -\frac{2n + m}{d_R}. \tag{2.9}$$

(2.10)

Here d_R is the greatest commond divisor (gcd) of $(2m + n)$ and $(2n + m)$. The length of the translation vector, T, is then given by

$$T = |\mathbf{T}| = \sqrt{3}L/d_R. \tag{2.11}$$

The unit cell of a SWNT is defined as the area covered by $\mathbf{C}_h$ and $\mathbf{T}$. It is given by

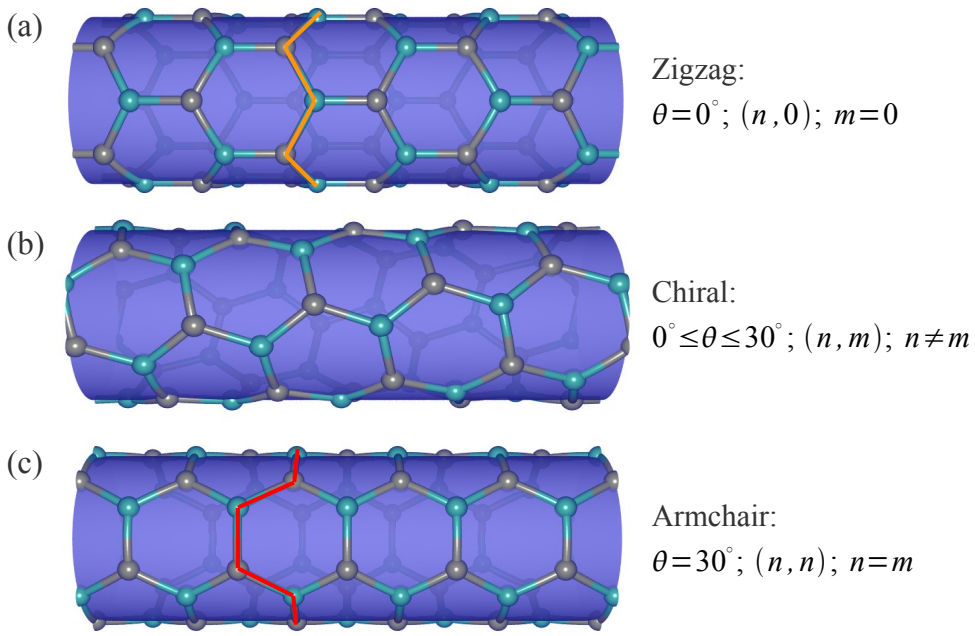

Figure 2-3: Classification of carbon nanotubes: (a) zigzag, (b) chiral, (c) armchair SWNTs. From left to right, the chiral index of each SWNT above is $(5,0)$, $(4,2)$, $(3,3)$, respectively. In (a) and (c), orange and red solid lines are intended to emphasize "zigzag" and "armchair" structures, respectively.

the magnitude of the vector product of $\mathbf{C}_h$ and $\mathbf{T}$. The number of hexagons per unit cell of the SWNT, N, is obtained by dividing the area of the SWNT unit cell with the area of the hexagonal unit cell in the graphene sheet:

$$N = \frac{|\mathbf{C}_h \times \mathbf{T}|}{\mathbf{a}_1 \times \mathbf{a}_2} = \frac{2(n^2 + nm + m^2)}{d_R}. \tag{2.12}$$

All the basic structural parameters of the SWNT are shown in Fig. 2-2. The SWNT can then be classified according to its (n, m) or θ value (see Fig. 2-3). This classification is based on the symmetry of the SWNT. There are three types of carbon nanotubes: zigzag, chiral, and armchair nanotubes. Chiral SWNTs exhibit a spiral symmetry whose mirror image cannot be superposed onto the original one. Zigzag and armchair SWNTs have mirror images that are identically the same as the original ones. The names of of armchair and

Fig. 2-3: fig/fch2-swnt.pdf

zigzag arise from the shape of the cross-sectional ring in the circumferential direction of the SWNTs. We then have various SWNT geometries that can change diameter, chirality, and also cap structures, giving rich physical properties of carbon nanotubes.

While the 1D unit cell of a SWNT in real space is expressed by $\mathbf{C}_h$ and $\mathbf{T}$, the corresponding vectors in reciprocal space are the vectors $\mathbf{K}_1$ along the tube circumference and $\mathbf{K}_2$ along the tube axis. Since nanotubes are 1D materials, only $\mathbf{K}_2$ is a reciprocal lattice vector. $\mathbf{K}_1$ gives discrete k values in the direction of $\mathbf{C}_h$. Expressions for $\mathbf{K}_1$ and $\mathbf{K}_2$ are obtained from their relations with $\mathbf{C}_h$ and $\mathbf{T}$:

$$\mathbf{C}_h \cdot \mathbf{K}_1 = 2\pi, \quad \mathbf{T} \cdot \mathbf{K}_1 = 0, \tag{2.13}$$

$$\mathbf{C}_h \cdot \mathbf{K}_2 = 0, \quad \mathbf{T} \cdot \mathbf{K}_2 = 2\pi. \tag{2.14}$$

It follows,

$$\mathbf{K}_1 = \frac{1}{N}(-t_2\mathbf{b}_1 + t_1\mathbf{b}_2), \mathbf{K}_2 = \frac{1}{N}(m\mathbf{b}_1 - n\mathbf{b}_2), \tag{2.15}$$

where $\mathbf{b}_1$ and $\mathbf{b}_2$ are the reciprocal lattice vectors of graphene. In Fig. 2-4, $\mathbf{K}_1$ and $\mathbf{K}_2$ are shown for the $(4, 2)$SWNT.

Fig. 2-4: fig/fch2-bz.pdf

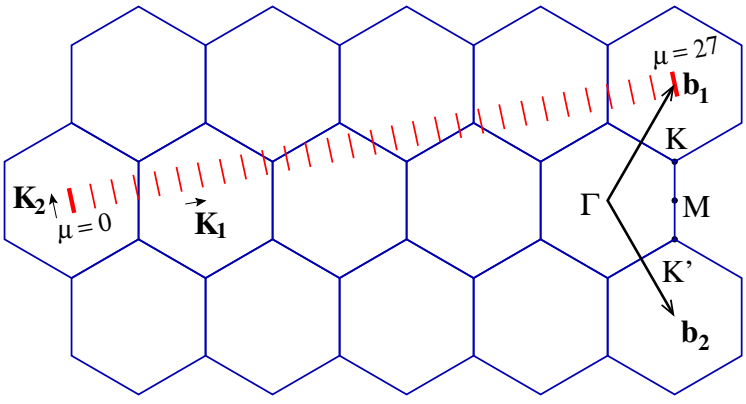

Figure 2-4: The reciprocal lattice vectors $\mathbf{K}_1$ and $\mathbf{K}_2$, and the Brillouin zone of a $(4, 2)$ SWNT represented by the set of $N = 28$ parallel cutting lines. The vectors $\mathbf{K}_1$ and $\mathbf{K}_2$ in reciprocal space correspond to $\mathbf{C}_h$ and $\mathbf{T}$ in real space, respectively. The cutting lines are labeled by the integer angular momentum index μ.

The allowed wave vector $\mathbf{k}$ of a SWNT is

$$\mathbf{k} = \mu\mathbf{K}_1 + k\frac{\mathbf{K}_2}{|\mathbf{K}_2|} \tag{2.16}$$

where $\mu = 0, 1, \ldots, N-1$ is the "cutting line" index, and k is in the range of $-\pi/T < k < \pi/T$. The length of $\mathbf{K}_1$ and $\mathbf{K}_2$ are given by:

$$|\mathbf{K}_1| = \frac{2\pi}{L} = \frac{2}{d_t}, \quad |\mathbf{K}_2| = \frac{2\pi}{T}. \tag{2.17}$$

The unit cell of the SWNT contains N hexagons, then the first Brillouin zone of the SWNT consists of N cutting lines. Therefore, N parallel cutting lines are related to the discrete value of the angular momentum μ, and the cutting line length $\mathbf{K}_2$ determines the periodicity of the 1D momentum k.

2.2 Tight-binding framework

The electronic dispersion relations of SWNTs are derived from those of a graphene sheet. The tight-binding model is reviewed here, starting from a simple tight-binding (STB) model. In a later section, the extended tight-binding (ETB) model that gives a good agreement with some optical spectroscopy measurements are described.

The electronic dispersion relations of a graphene sheet are obtained by solving the single particle Schrödinger equation:

$$H\Psi^b(\mathbf{k}, \mathbf{r}, t) = i\hbar\frac{\partial}{\partial t}\Psi^b(\mathbf{k}, \mathbf{r}, t)\,, \tag{2.18}$$

where $H = T + V(\mathbf{r})$ is the single-particle Hamiltonian, T is the kinetic energy operator, $V(\mathbf{r})$ is the effective periodic potential, $\Psi^b(\mathbf{k}, \mathbf{r}, t)$ is the one-electron wavefunction, b is the band index, $\mathbf{k}$ is the electron wavevector, $\mathbf{r}$ is the spatial coordinate, and t is time. The electron wavefunction $\Psi^b(\mathbf{k}, \mathbf{r}, t)$ is approximated by a linear combination of atomic orbitals

(LCAO) in terms of Bloch functions:

$$\begin{aligned}\Psi^b(\mathbf{k},\mathbf{r},t) &= \exp\left(-iE^b(\mathbf{k})t/\hbar\right)\sum_{so} C^b_{so}(\mathbf{k})\Phi_{so}(\mathbf{k},\mathbf{r})\,,\\ \Phi_{so}(\mathbf{k},\mathbf{r}) &= \frac{1}{\sqrt{U}}\sum_{u}^{U}\exp\left(i\mathbf{k}\mathbf{R}_{us}\right)\phi_o(\mathbf{r}-\mathbf{R}_{us})\,,\end{aligned} \tag{2.19}$$

where $E^b(\mathbf{k})$ is the one-electron energy, $C^b_{so}(\mathbf{k})$ is the Bloch amplitude, $\Phi_{so}(\mathbf{k},\mathbf{r})$ is the Bloch wavefunction, $\phi_o(\mathbf{r})$ is the atomic orbital, $\mathbf{R}_{us}$ is the atomic coordinate, the index $u = 1,\ldots,U$ is for all the U unit cells in a graphene sheet, the index $s = \mathrm{A},\mathrm{B}$ labels the two inequivalent atoms in the unit cell, and the index $o = 1s, 2s, 2p_x, 2p_y, 2p_z$ gives the atomic orbitals of a carbon atom.

The stationary Schrödinger equation for the Bloch amplitudes $C^b_{so}(\mathbf{k})$ can be written in the matrix form:

$$\sum_{so} H_{s'o'so}(\mathbf{k})C^b_{so}(\mathbf{k}) = \sum_{so} E^b(\mathbf{k})S_{s'o'so}(\mathbf{k})C^b_{so}(\mathbf{k})\,, \tag{2.20}$$

where the Hamiltonian $H_{s'o'so}(\mathbf{k})$ and overlap $S_{s'o'so}(\mathbf{k})$ matrices are given by:

$$\begin{aligned}H_{s'o'so}(\mathbf{k}) &= \sum_{u}^{U}\exp\left(i\mathbf{k}\left(\mathbf{R}_{us}-\mathbf{R}_{u's'}\right)\right)\int \phi^*_{o'}(\mathbf{r}-\mathbf{R}_{u's'})H\phi_o(\mathbf{r}-\mathbf{R}_{us})d\mathbf{r}\,,\\ S_{s'o'so}(\mathbf{k}) &= \sum_{u}^{U}\exp\left(i\mathbf{k}\left(\mathbf{R}_{us}-\mathbf{R}_{u's'}\right)\right)\int \phi^*_{o'}(\mathbf{r}-\mathbf{R}_{u's'})\phi_o(\mathbf{r}-\mathbf{R}_{us})d\mathbf{r}\,,\end{aligned} \tag{2.21}$$

and the index u' labels the unit cell under consideration. The orthonormality condition for the electron wavefunction of Eq. (2.19) becomes:

$$\int \Psi^{b'*}(\mathbf{k},\mathbf{r},t)\Psi^b(\mathbf{k},\mathbf{r},t)d\mathbf{r} = \sum_{s'o'}\sum_{so} C^{b'*}_{s'o'}(\mathbf{k})S_{s'o'so}(\mathbf{k})C^b_{so}(\mathbf{k}) = \delta_{b'b}\,. \tag{2.22}$$

To evaluate the integrals in Eq. (2.21), the effective periodic potential $V(\mathbf{r})$ in the single particle Hamiltonian H of Eq. (2.18) is expressed by a sum of the effective spherically-

symmetric potentials $U(\mathbf{r}-\mathbf{R}_{u''s''})$ centered at the atomic sites $\mathbf{R}_{u''s''}$:

$$V(\mathbf{r}) = \sum_{u''s''} U(\mathbf{r}-\mathbf{R}_{u''s''})\,. \tag{2.23}$$

The Hamiltonian matrix $H_{s'o'so}(\mathbf{k})$ then contains the three-center integrals that involve two orbitals $\phi^*_{o'}(\mathbf{r}-\mathbf{R}_{u's'})$ and $\phi_o(\mathbf{r}-\mathbf{R}_{us})$ at two different atomic sites $\mathbf{R}_{u's'}$ and $\mathbf{R}_{us}$, while the potential $U(\mathbf{r}-\mathbf{R}_{u''s''})$ originates from a third atomic site $\mathbf{R}_{u''s''}$. On the other hand, the overlap matrix $S_{s'o'so}(\mathbf{k})$ contains two-center integrals only. Neglecting the three-center integrals in $H_{s'o'so}(\mathbf{k})$, the remaining two-center integrals in both $H_{s'o'so}(\mathbf{k})$ and $S_{s'o'so}(\mathbf{k})$ can be parameterized as functions of the interatomic vector $\mathbf{R}=\mathbf{R}_{us}-\mathbf{R}_{u's'}$ and of the symmetry and relative orientation of the atomic orbitals $\phi^*_{o'}(\mathbf{r})$ and $\phi_o(\mathbf{r})$:

$$\begin{aligned}
\varepsilon_o &= \int \phi^*_o(\mathbf{r}) H \phi_o(\mathbf{r}) d\mathbf{r}\,,\\
t_{o'o}(\mathbf{R}) &= \int \phi^*_{o'}(\mathbf{r})\left(T + U(\mathbf{r}) + U(\mathbf{r}-\mathbf{R})\right)\phi_o(\mathbf{r}-\mathbf{R}) d\mathbf{r}\,,\\
s_{o'o}(\mathbf{R}) &= \int \phi^*_{o'}(\mathbf{r})\phi_o(\mathbf{r}-\mathbf{R}) d\mathbf{r}\,,
\end{aligned} \tag{2.24}$$

where ε_o is the atomic orbital energy, $t_{o'o}(\mathbf{R})$ is the transfer integral, and $s_{o'o}(\mathbf{R})$ is the overlap integral. A numerical calculation of parameters ε_o, $t_{o'o}(\mathbf{R})$, and $s_{o'o}(\mathbf{R})$ defines the non-orthogonal tight-binding model. Within the orthogonal tight-binding model, $s_{o'o}(\mathbf{R})$ is set to zero.

2.2.1 Graphene dispersion relations

In the STB model, we neglect the σ molecular orbitals and the long-range atomic interactions, $R > a_{\mathrm{CC}}$. The STB model thus has three parameters: the atomic orbital energy ε_{2p}, the transfer integral $t_{\pi\pi}(a_{\mathrm{CC}})$, and the overlap integral $s_{\pi\pi}(a_{\mathrm{CC}})$. The transfer and overlap integrals will simply be referred to as t, and s, respectively.

To construct the Hamiltonian $H_{s'o'so}(\mathbf{k})$ and overlap $S_{s'o'so}(\mathbf{k})$ matrices of Eq. (2.20), consider the nearest-neighbor interactions ($R = a_{\mathrm{CC}}$) in the unit cell of a graphene sheet.

The unit cell contains two atoms, A and B, each of which has three nearest neighbors of the opposite atom type. The absence of nearest-neighbor interactions within the same A or B sublattice gives the diagonal Hamiltonian and overlap matrix elements, $H_{\mathrm{A}\pi\mathrm{A}\pi} = H_{\mathrm{B}\pi\mathrm{B}\pi} = \varepsilon_{2p}$ and $S_{\mathrm{A}\pi\mathrm{A}\pi} = S_{\mathrm{B}\pi\mathrm{B}\pi} = 1$, independent of the transfer t and overlap s integrals. For the $H_{\mathrm{A}\pi\mathrm{B}\pi}$ and $S_{\mathrm{A}\pi\mathrm{B}\pi}$ matrix elements, the interatomic vectors $\mathbf{R}$ from atom A to its three nearest-neighbors in Eq. (2.20) are given by $(\mathbf{a}_1 + \mathbf{a}_2)/3$, $(\mathbf{a}_1 - 2\mathbf{a}_2)/3$, and $(\mathbf{a}_2 - 2\mathbf{a}_1)/3$. Substituting these vectors into Eq. (2.20), one can obtain $H_{\mathrm{A}\pi\mathrm{B}\pi} = tf(\mathbf{k})$ and $S_{\mathrm{A}\pi\mathrm{B}\pi} = sf(\mathbf{k})$, where $f(\mathbf{k})$ is the sum of the phase factors over the nearest neighbors given by

$$f(\mathbf{k}) = \exp\left(i\frac{k_x a}{\sqrt{3}}\right) + \exp\left(-i\frac{k_x a}{2\sqrt{3}} + i\frac{k_y a}{2}\right) + \exp\left(-i\frac{k_x a}{2\sqrt{3}} - i\frac{k_y a}{2}\right). \tag{2.25}$$

The $H_{\mathrm{B}\pi\mathrm{A}\pi}$ and $S_{\mathrm{B}\pi\mathrm{A}\pi}$ matrix elements are derived in a similar way. The interatomic vectors $\mathbf{R}$ have the opposite signs, giving $H_{\mathrm{B}\pi\mathrm{A}\pi} = tf^*(\mathbf{k})$ and $S_{\mathrm{B}\pi\mathrm{A}\pi} = sf^*(\mathbf{k})$. The Schrödinger equation in the matrix form, Eq. (2.20), can be written as

$$\begin{pmatrix} \varepsilon_{2p} & tf(\mathbf{k}) \\ tf^*(\mathbf{k}) & \varepsilon_{2p} \end{pmatrix} \begin{pmatrix} C^b_{\mathrm{A}\pi}(\mathbf{k}) \\ C^b_{\mathrm{B}\pi}(\mathbf{k}) \end{pmatrix} = E^b(\mathbf{k}) \begin{pmatrix} 1 & sf(\mathbf{k}) \\ sf^*(\mathbf{k}) & 1 \end{pmatrix} \begin{pmatrix} C^b_{\mathrm{A}\pi}(\mathbf{k}) \\ C^b_{\mathrm{B}\pi}(\mathbf{k}) \end{pmatrix}. \tag{2.26}$$

Solving this secular equation yields the energy eigenvalues:

$$E^v(\mathbf{k}) = \frac{\varepsilon_{2p} + tw(\mathbf{k})}{1 + sw(\mathbf{k})}, \quad E^c(\mathbf{k}) = \frac{\varepsilon_{2p} - tw(\mathbf{k})}{1 - sw(\mathbf{k})}, \tag{2.27}$$

where the band index $b = v, c$ indicates the valence and conduction bands, $t < 0$, and $w(\mathbf{k})$ is the absolute value of the phase factor $f(\mathbf{k})$, i.e., $w(\mathbf{k}) = \sqrt{f^*(\mathbf{k})f(\mathbf{k})}$:

$$w(\mathbf{k}) = \sqrt{1 + 4\cos\frac{\sqrt{3}k_x a}{2}\cos\frac{k_y a}{2} + 4\cos^2\frac{k_y a}{2}}. \tag{2.28}$$

According to Eq. (2.27), the atomic orbital energy ε_{2p} is an arbitrary reference point in the orthogonal STB model ($s = 0$), while ε_{2p} is a relevant parameter in the non-orthogonal STB model ($s \neq 0$).

Fitting the dispersion relations of the graphene sheet given by Eq. (2.27) to the energy values obtained from an *ab initio* calculation gives the values of the transfer integral $t = -3.033\,\mathrm{eV}$ and overlap integral $s = 0.129$, and set the atomic orbital energy equal to zero of the energy scale, $\varepsilon_{2p} = 0\,\mathrm{eV}$ [4]. Fig. 2-5 (a) shows the dispersion relations of the graphene sheet given by Eq. (2.27) with the above parameters throughout the entire area of the first Brillouin zone. The lower (valence) band is completely filled with electrons in the ground state, while the upper (conduction) band is completely empty of electrons in the ground state.

Unlike most semiconductors, the band structure of a graphene sheet shows linear dispersion relations around the K and K′ points near the Fermi level, as can be seen in Fig. 2-5(b). The electron wavevector around the K point in the first Brillouin zone can be written in the form $k_x = \Delta k_x$ and $k_y = -4\pi/(3a) + \Delta k_y$, where Δk_x and Δk_y are small compared to $1/a$. Substituting this wavevector into Eq. (2.28) and making the expansion in a power series in $\Delta k_x a$ and $\Delta k_y a$ up to the second order, one can obtain $w = \frac{\sqrt{3}}{2}\Delta k a$, where $\Delta k = \sqrt{\Delta k_x^2 + \Delta k_y^2}$ is the distance from the electron wavevector to the K point. Substituting w into Eq. (2.27) gives the electronic dispersion relations in the valence and conduction

Fig. 2-5: fig/fch2-piband.pdf

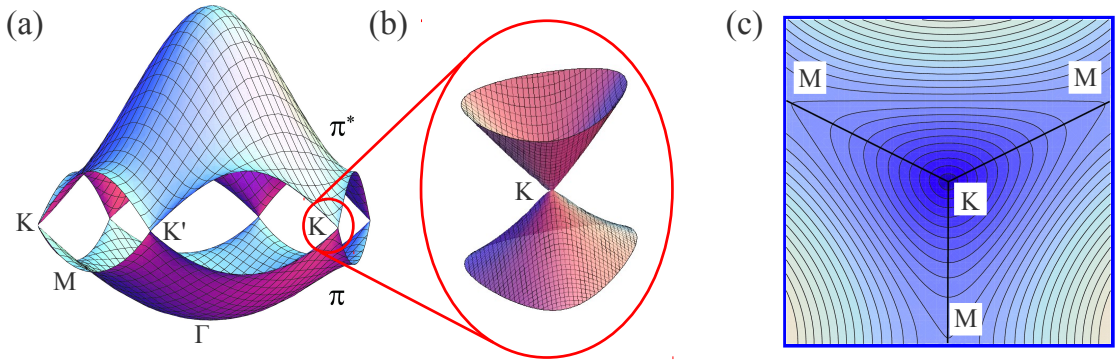

Figure 2-5: The π bands of graphene within the simple tight-binding method. In (a), the energy dispersion is shown throughout the whole region of the Brillouin zone. (b) Near the K point, the energy dispersion relation is approximately linear, showing two symmetric cone shapes, the so-called Dirac cones. (c) Contour plot of the energy dispersion near the K point. The tight-binding parameters used here are $\epsilon_{2p} = 0\,\mathrm{eV}$, $t = -3.033\,\mathrm{eV}$, and $s = 0.129$.

bands:

$$E^v(\Delta k) = \varepsilon_{2p} - \frac{\sqrt{3}}{2}(\varepsilon_{2p}s - t)\, a\, \Delta k\,, \quad E^c(\Delta k) = \varepsilon_{2p} + \frac{\sqrt{3}}{2}(\varepsilon_{2p}s - t)\, a\, \Delta k\,, \tag{2.29}$$

which are linear in Δk. The linear dispersion relations near the Fermi level suggest that the effective mass approximation of the non-relativistic Schrödinger equation used for conventional semiconductors with parabolic energy bands is not applicable to a graphene sheet. The conducting π electrons in a graphene sheet mimic massless particles whose behavior is described by the relativistic Dirac equation. Furthermore, the linear dispersion relations increase the mobility of the conducting π electrons in a graphene sheet compared to conventional semiconductors. In contrast to the π electrons, the σ electrons are involved in covalent bonds, and therefore are not mobile. Indeed, the σ energy bands lie several eV away from the Fermi level, as obtained by solving Eq. (2.20) for the σ molecular orbitals. In Fig. 2-5(c), the contour plot of the energy dispersion near the K point is shown. The energy surface changes from circle to triangle with increasing distance from the K point, giving rise to the so-called trigonal warping effect [7], which strongly affects the optical transitions in SWNTs.

2.2.2 Nanotube electronic structure

Now the electronic structure of a SWNT can be derived from the energy dispersion calculation of graphene. The allowed wave vectors $\mathbf{k}$ (the cutting lines) around the SWNT circumference become quantized. The energy dispersion relations of the SWNT are then given by the corresponding energy dispersion relations of graphene along the cutting lines. When the 1D cutting lines $\mu\mathbf{K}_1 + k\mathbf{K}_2/|\mathbf{K}_2|$ of a SWNT in Eq. 2.16 are superimposed on the 2D electronic energy dispersion surface of the graphene sheet in Eq. 2.27, N pairs of energy dispersion relations of the SWNT, $E^b_{\mathrm{SWNT}}(\mu, k)$, are obtained:

$$E^b_{\mathrm{SWNT}}(\mu, k) = E^b_{\mathrm{2D}}\left(\mu\mathbf{K}_1 + k\frac{\mathbf{K}_2}{|\mathbf{K}_2|}\right), \quad \left(\mu = 0, 1, \ldots, N-1; -\frac{\pi}{T} < k < \frac{\pi}{T}\right). \tag{2.30}$$

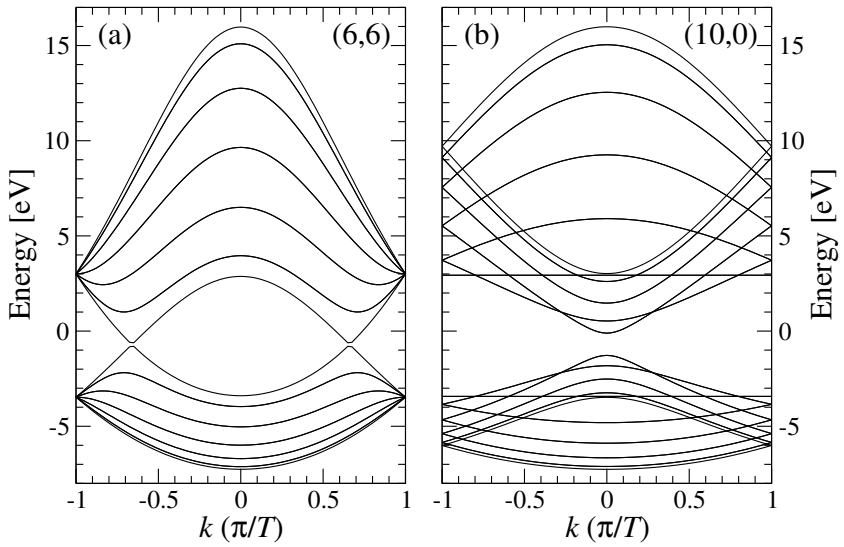

Figure 2-6: Examples of 1D energy dispersion relations of SWNTs: (a) armchair $(6, 6)$, and (b) zigzag $(10, 0)$ SWNTs. No bandgaps can be seen in (a), thus the SWNT is metallic, whereas the SWNT in (b) is semiconducting because there is an open gap.

For a particular (n, m) SWNT, if a cutting line passes through K or K$'$ point of the Brillouin zone of graphene, where the valence and conduction bands touch to each other, the 1D energy bands of the SWNT have a zero energy gap, therefore, they become metallic. However, if a cutting line does not pass through K or K$'$, the (n, m) is semiconducting with a finite energy gap. Figure 2-6 gives two examples of the SWNT dispersion relations.

As shown in Fig. 2-7(a), if we project the $\mathbf{\Gamma K}$ vector pointing toward the K point onto the $\mathbf{K}_1$ direction perpendicular to the cutting lines, that can be denoted by $\mathbf{\Gamma Y} = \mathbf{\Gamma K} \cdot \mathbf{K}_1$, we can find:

$$\frac{\mathbf{\Gamma K}}{\mathbf{K}_1\mathbf{K}_1} = \frac{\frac{1}{3}(2\mathbf{b}_1 + \mathbf{b}_2) \cdot \frac{1}{N}(t_1\mathbf{b}_2 - t_2\mathbf{b}_1)}{\frac{1}{N}(t_1\mathbf{b}_2 - t_2\mathbf{b}_1)\frac{1}{N}(t_1\mathbf{b}_2 - t_2\mathbf{b}_1)} \tag{2.31}$$

$$= \frac{2n + m}{3}, \tag{2.32}$$

If $(2n + m)/3$ is an integer, $\mathbf{\Gamma K}$ has an integer number of $\mathbf{K}_1$ components, so that one of

Fig. 2-6: fig/fch2-dis.pdf
Fig. 2-7: fig/fch2-class.pdf
Fig. 2-8: fig/fch2-famnum.pdf

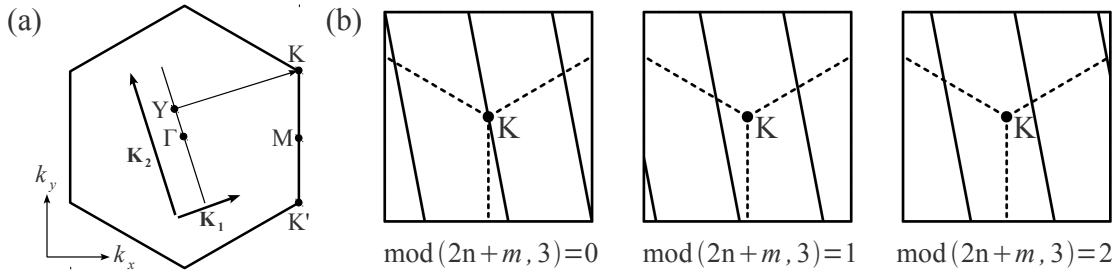

Figure 2-7: (a) Condition for metallic energy bands is related to the ratio of the length of vector **YK** to that of $\mathbf{K}_1$. If the ratio is an integer, metallic energy bands are obtained [4]. (b) Three possible configurations of the cutting lines in the vicinity of the K point depending on the value of $\mathrm{mod}(2n+m, 3)$. From left to right, the nanotube type is M- (metallic), S1- (type-I semiconducting), and S2- (type-II semiconducting) SWNT, respectively. The solid lines represent the cutting lines and the dashed lines indicate the KM directions, which are the boundaries of the first Brillouin zone of the SWNT.

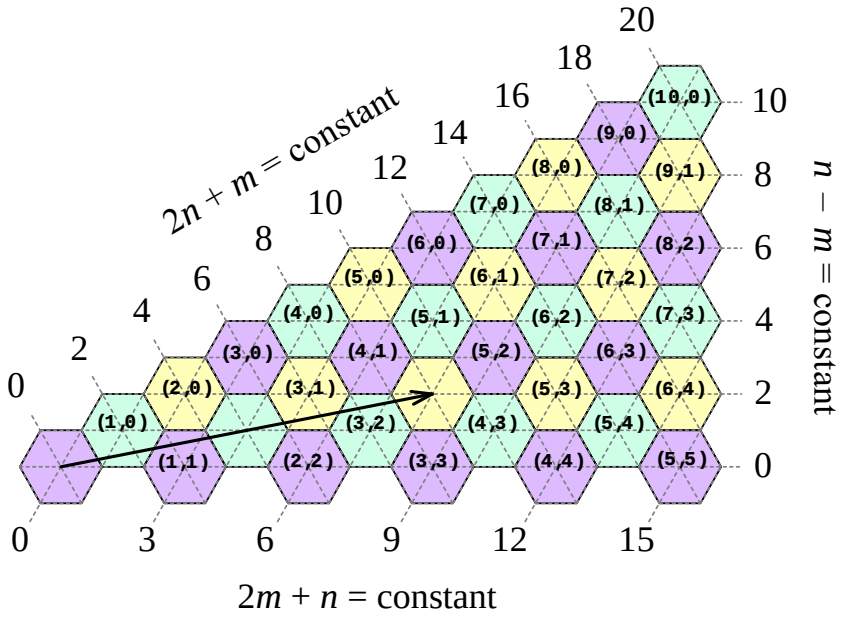

Figure 2-8: Nanotubes family classification on the unrolled graphene sheet for the nanotubes of diameter less than 1 nm. The (n, m) indices written in the hexagons represent the chiral vectors pointing to the centers of the hexagons. Here the chiral vector of a $(4, 2)$ SWNT is shown by an arrow. The dashed lines represent the families of constant $2n + m$, $n - m$, and $2m + n$ for each family. The magenta, light yellow, and cyan hexagons correspond to the chiral vectors of M-, S1-, and S2-SWNTs, respectively.

the cutting lines passes through the K point, hence giving a metallic SWNT. If $(2n+m)/3$ is not an integer, i.e, the residual is 1 or 2, the K point lies at 1/3 or 2/3 of the spacing between two adjacent cutting lines near the K point, hence giving a semiconducting SWNT, as shown in Fig. 2-7(b). These three types of SWNTs are referred to as M-, S1-, and S2-SWNTs, respectively:

$$\text{M} \quad : \quad \text{mod}(2n+m, 3) = 0, \tag{2.33}$$

$$\text{S1} \quad : \quad \text{mod}(2n+m, 3) = 1, \tag{2.34}$$

$$\text{S2} \quad : \quad \text{mod}(2n+m, 3) = 2. \tag{2.35}$$

The S1- and S2-SWNTs are often written as type-I and type-II semiconducting SWNTs. There are also other metallicity notations frequently used in the nanotube research community depending on the value of $\text{mod}(n-m, 3)$ as follows:

$$\text{mod}\,0 \quad : \quad \text{mod}(n-m, 3) = 0, \tag{2.36}$$

$$\text{mod}\,1 \quad : \quad \text{mod}(n-m, 3) = 1, \tag{2.37}$$

$$\text{mod}\,2 \quad : \quad \text{mod}(n-m, 3) = 2. \tag{2.38}$$

With a simple algebra, it can be shown that mod 0, mod 1, and mod 2 SWNTs are the same as M-, S2-, S1-SWNTs, respectively.

In Fig. 2-8, the chiral vectors for M-, S1-, and S2-SWNTs are shown. Within the triangular graphene sheet, the diagonal lines of each hexagon are connected to the diagonal lines of the adjacent hexagons, shown by the dashed lines in Fig. 2-8. These lines with constant values of $(2n+m)$, $(2m+n)$, and $(n-m)$ are called the family lines. Especially for the $(2n+m)$ families, the SWNTs which belong to the same $(2n+m)$ have the closest diameters, compared to the $(2m+n)$ or $(n-m)$ families, as obviously can be seen in Fig. 2-9.

Fig. 2-9: fig/fch2-2nmfam.pdf

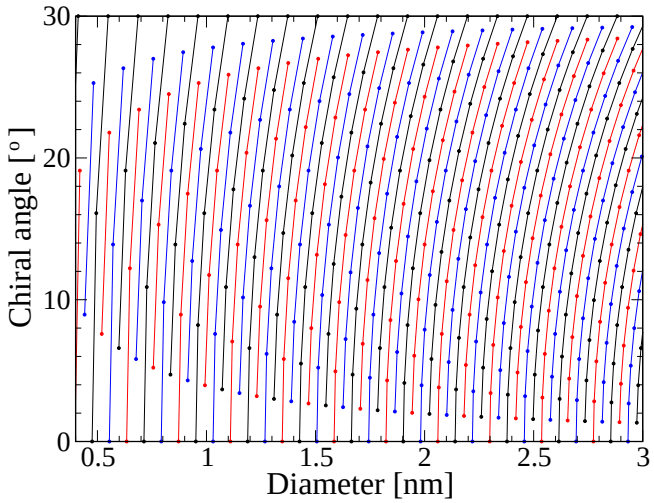

Figure 2-9: Chiral angle (θ) versus diameter (d_t) of all SWNTs in the range of $0.5 < d_t < 3\,\text{nm}$. Nanotubes of the same family number ($2n + m$) are connected by lines. Up to $d_t \approx 1.2\,\text{nm}$, the constant $2n + m$ nanotubes have similar diameters.

2.3 Density of states and transition energies

The electronic density of states (DOS) or the number of available electrons for a given energy interval is especially very important for understanding optical properties of materials. The DOS is known to depend on the dimension of the materials. For parabolic bands found in most semiconductors, the DOS rises as the square root of the energy above the energy bottom E_0 in the 3D cases such as diamond and graphite, $g(E) \propto (E - E_0)^{1/2}$. For a 1D system such as SWNT, E_0 is equal to the subband edge energy E_i^b, where the DOS magnitude becomes singular, known as the van-Hove singularity (VHS). The presence of VHSs in the DOS of SWNTs has a great impact on their optical properties, a significant enhancement in the SWNT response is observed when the excitation energy for the probe matches one of the VHSs in the DOS in the valence and conduction bands of the SWNT. For example, optical absorption is strongly enhanced when the photon energy is in resonance with the allowed transition between two VHSs in the valence and conduction bands. This enhancement is generally interpreted in terms of the joint density of electronic states (JDOS) which takes into account the dipole selection rules. The optical transitions should conserve both angular and linear momenta in SWNTs, thus the transitions are vertical, as shown in Fig. 2-10.

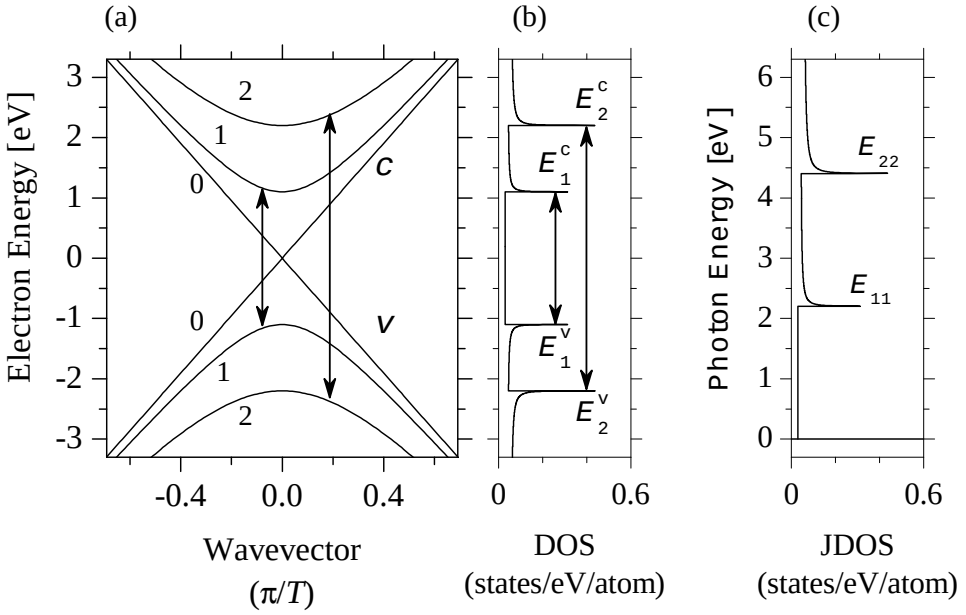

Figure 2-10: (a) The dispersion relations and (b) density of electronic states DOS of the $(15, 0)$ SWNT. The arrows show the allowed optical transitions between the first and second valence and conduction subbands. (c) The joint density of states (JDOS) of the $(15, 0)$ SWNT. The labels E_{11} (E_{22}) corresponds to the transition between E_1^v and E_1^c (E_2^v and E_2^c) shown in (b).

The optical response of SWNTs is dominated by the VHSs in the JDOS labeled by E_{ii}. The optical transition energies E_{ii} for $i = 1, 2, 3, \ldots$ and for all the possible (n, m) SWNTs are summarized in the Kataura plot [6] as a function of the SWNT diameter d_t. The Kataura plot is a useful tool for analyzing Raman spectra of SWNTs, since the frequency of the Raman-active radial-breathing phonon mode ω_{RBM} is inversely proportional to d_t. In Fig. 2-11(a), the Kataura plot calculated within the STB model is shown, in which the transition energies are interpreted as the energy gaps between i-th VHSs in the conduction and valence bands. The same STB Kataura plot is shown in Fig. 2-11 (b) as a function of the inverse SWNT diameter $1/d_t$, which is more convenient for direct comparison with experiments, since $1/d_t$ is proportional to ω_{RBM}. Furthermore, the $1/d_t$ scale allows us to explore the small d_t region ($d_t < 1.2\,\mathrm{nm}$), which has a lower density of (n, m) indices. As one can see

Fig. 2-10: fig/fch2-dos.pdf

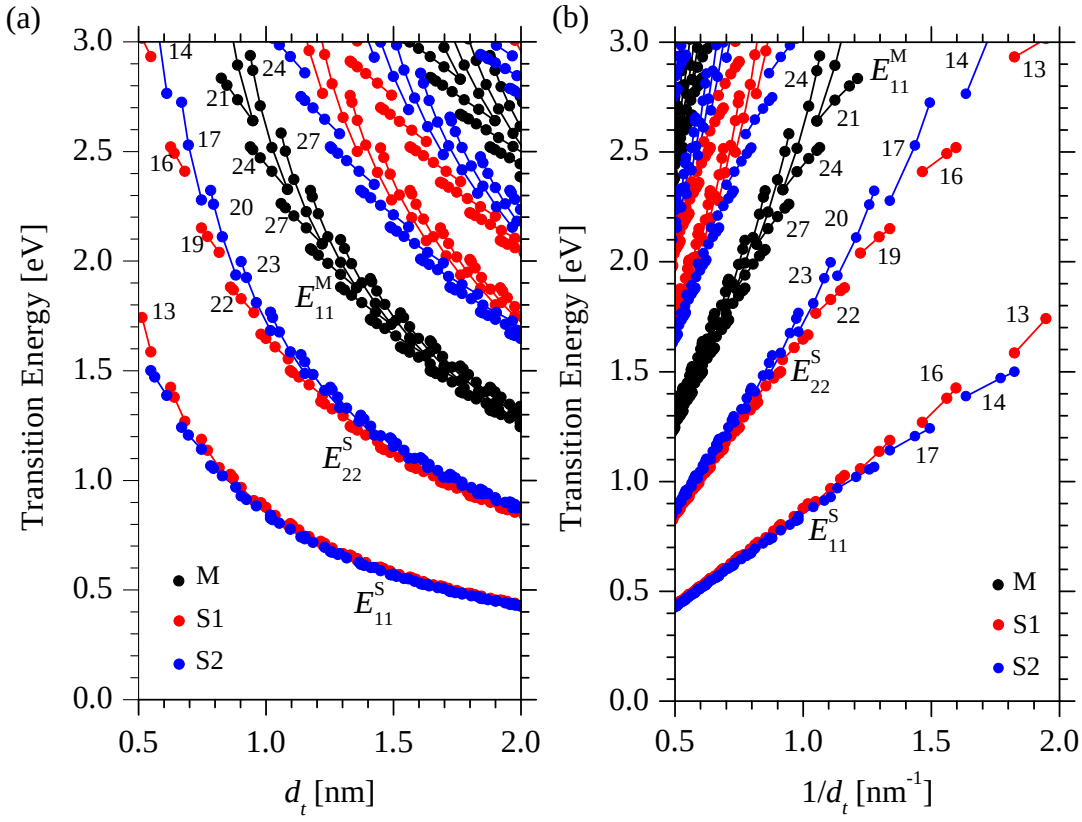

Figure 2-11: The optical transition energies E_{ii} for $i = 1, 2, 3, \ldots$ and for all possible (n, m) SWNTs in the range of $0.5 < d_t < 2.0\,\text{nm}$ calculated within the STB model as a function of (a) SWNT diameter d_t, and (b) inverse diameter $1/d_t$, known as the Kataura plot. Black, red, and blue dots correspond to M-, S1-, and S2 SWNTs, respectively. The constant $2n+m$ families are connected by lines.

from Fig. 2-11, the E_{ii} energies for M-, S1-, and S2-SWNTs show distinct behavior. Within the M-, S1-, and S2-types, the E_{ii} energies that belong to the families of constant $2n + m$ group together in the Kataura plot.

2.4 Extended tight-binding model

Recent E_{ii} measurements by photoluminiscence (PL) and resonance Raman spectroscopy (RRS) clearly indicate that the STB calculation is not sufficient to interpret the experimental

Fig. 2-11: fig/fch2-stbkat.pdf

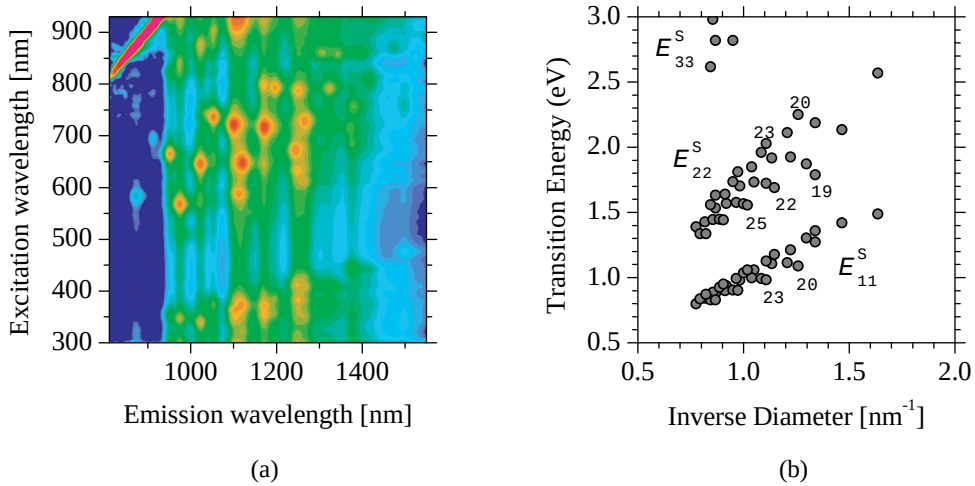

Figure 2-12: (a) 2D photoluminiscence (PL) map measured on wrapped HiPco SWNTs suspended by SDS surfactant in aqueous solution [36]. (b) The Kataura plot extracted from the PL map [28]. The numbers show the constant $2n + m$ families.

results. Figures 2-12 and 2-13 give the same E_{ii} energies for the same SWNT sample, that is HiPco SWNTs suspended by SDS surfactant in aqueous solution. The experimental Kataura plots in Figs. 2-12(b) and 2-13(b) differ from the theoretical STB Kataura plot in two different directions: in the large diameter limit and in the small diameter limit.

In the large d_t limit, the ratio of E_{22}^{S} to E_{11}^{S} reaches 1.8 in the experimental Kataura plots, while the same ratio goes to 2 in the theoretical Kataura plot [36]. The ratio problem is an indication of the many-body interactions related to the excitons, that will be discussed in the next chapter. In the small d_t limit, the families of constant $2n + m$ deviate from the mean E_{ii} energy bands in the experimental Kataura plots, while the family spread in the theoretical Kataura plot remains relatively moderate [28]. In search for the origin of the family spread, we reconsider the limitations of the STB model discussed previously. Within the STB model, the long-range atomic interactions and the σ molecular orbitals are neglected. Meanwhile, the long-range atomic interactions are known to alternate the electronic band structure of the graphene sheet and SWNTs. On the other hand, the σ

Fig. 2-12: fig/fch2-pl.pdf
Fig. 2-13: fig/fch2-rrs.pdf

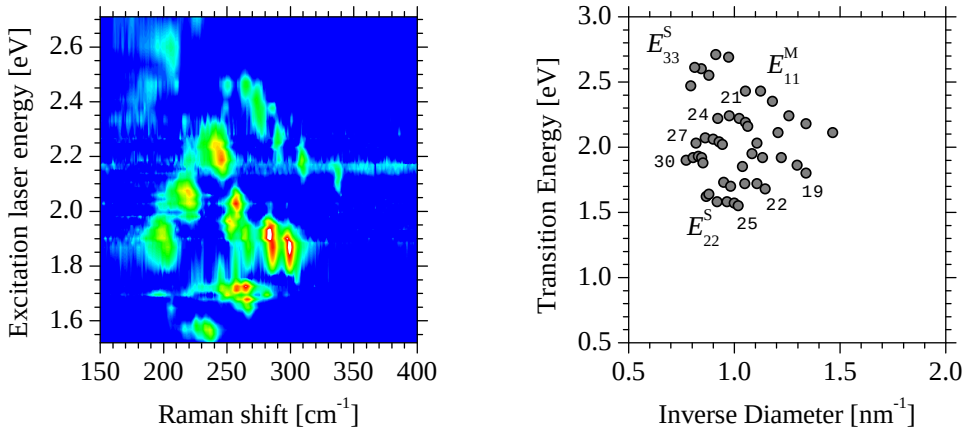

Figure 2-13: (a) The resonance Raman spectral density map in the frequency range of the RBM measured on wrapped HiPco SWNTs suspended by SDS surfactant in aqueous solution[37]. (b) The Kataura plot extracted from the map in (a). The numbers show the constant $2n + m$ families.

molecular orbitals are irrelevant in the graphene sheet and large diameter SWNTs as they lie far away in energy from the Fermi level. In small diameter SWNTs, however, the curvature of the SWNT sidewall changes the lengths of the interatomic bonds and the angles between them. This leads to the rehybridization of the σ and π molecular orbitals, which affects the band structure of π electrons near the Fermi level. Furthermore, the σ-π rehybridization suggests that the geometrical structure of a small diameter SWNT deviates from the rolled up graphene sheet. A geometrical structure optimization must thus be performed to allow for atomic relaxation to equilibrium positions. This in turn affects the E_{ii} energies of the small diameter SWNTs.

The STB model is now extended by including the long-range atomic interactions and the σ molecular orbitals, and by optimizing the geometrical structure. The resulting model is referred to as the extended tight-binding model (ETB). Within the framework of the ETB model, we use the tight-binding parametrization determined from density-functional theory (DFT) employing the local-density approximation (LDA) and using a local orbital

Fig. 2-14: fig/fch2-etbkat.pdf

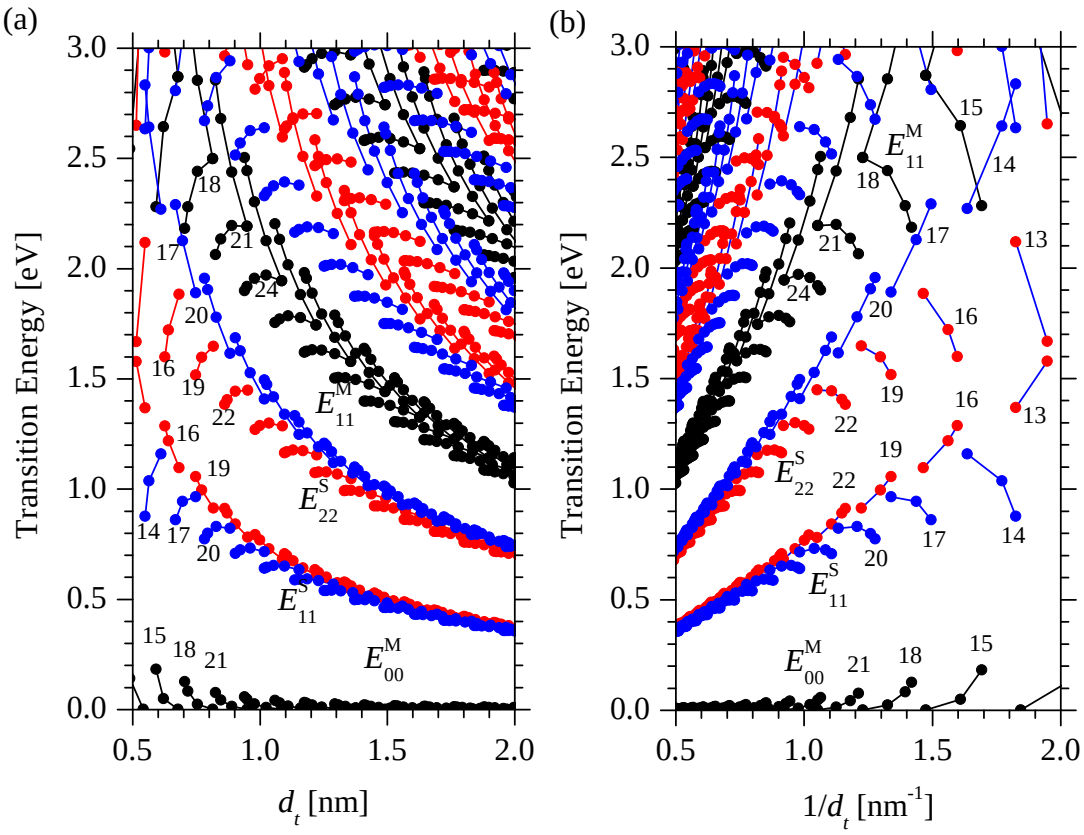

Figure 2-14: The ETB Kataura plot similar to the STB Kataura plot in Fig. 2-11 as a function of (a) SWNT diameter d_t, and (b) inverse diameter $1/d_t$. The ETB model takes into account the long-range atomic interactions, the curvature effects of small diameter SWNTs, and the optimized geometrical structures of the SWNTs. Black, red, and blue dots correspond to M-, S1-, and S2 SWNTs, respectively. The constant $2n + m$ families are connected by lines.

basis set [38]. The ETB model is discussed in detail by Samsonidze *et. al* [8]. The ETB Kataura plot shows a similar family spread to the PL and RRS experimental Kataura plots (see Fig. 2-14). The experimental family spread is concluded to be related to the relaxation of the geometrical structure of SWNTs. Although the family spread of the ETB model is in good agreement with the PL and RRS Kataura plots, it still deviates $200 - 300$ meV from the PL and RRS experiments. This deviations originates from the many-body effects and later can be confirmed in the exciton picture.

Chapter 3

Excitons in carbon nanotubes

Exciton effects in SWNTs are very important due to confinement of electrons and holes in the 1D system. Though in the previous chapter we have seen that the single particle (electron) model within the extended tight-binding (ETB) approximation can partially describe the optical transition energies, the presence of excitons in the real case cannot be neglected, as is indicated by the large exciton binding energy measured in the experiments [10, **?**]. Moreover, the many-body corrections can only be understood by taking into account the exciton effects. In this chapter, the methods for calculating the transition energies in the exciton picture are reviewed and some relevant results will be discussed. The electron-hole corrections are included via the Bethe-Salpeter equation and the calculation is again performed within the ETB approximation as the ETB model has been proven to accurately predict the electronic properties of SWNTs. This framework has been summarized into an exciton energy calculation package following the work by Jiang et al. [30] and Sato et al. [33]. The computer program is now maintained in our research group.

3.1 Bethe-Salpeter equation

Exciton is an electron-hole pair bound by a Coulomb interaction and thus localized either in real space or k space. But in solids, all wave functions are delocalized as the Bloch wave

functions. The wave vector of an electron ($\mathbf{k}_c$) or a hole ($\mathbf{k}_v$) is no longer a good quantum number. To create an exciton wave function from the electron and hole wave functions, the electron and hole Bloch functions at many ($\mathbf{k}_c$) and ($\mathbf{k}_v$) wave vectors have to be mixed. The mixing of different wavevectors by the Coulomb interaction is obtained by the so-called BetheSalpeter equation [39, 40, 30]:

$$\sum_{\mathbf{k}_c,\mathbf{k}_v} [(E(\mathbf{k}_c) - E(\mathbf{k}_v))\delta(\mathbf{k}'_c,\mathbf{k}_c)\delta(\mathbf{k}'_v,\mathbf{k}_v) + K(\mathbf{k}'_c\mathbf{k}'_v,\mathbf{k}_c\mathbf{k}_v)]\Psi^n(\mathbf{k}_c,\mathbf{k}_v) = \Omega_n\Psi^n(\mathbf{k}'_c,\mathbf{k}'_v), \quad (3.1)$$

where $E(\mathbf{k}_c)$ and $E(\mathbf{k}_v)$ are the quasi-electron and quasi-hole energies, respectively. The "quasiparticle" means that a Coulomb interaction is added to the single particle energy and the particle has a finite life time in an excited state. Ω_n and Ψ^n are the n-th excited state exciton energy and corresponding wave function.

The mixing term or kernel $K(\mathbf{k}'_c\mathbf{k}'_v,\mathbf{k}_c\mathbf{k}_v)$ is given by

$$K(\mathbf{k}'_c\mathbf{k}'_v,\mathbf{k}_c\mathbf{k}_v) = 2\delta_S K^x(\mathbf{k}'_c\mathbf{k}'_v,\mathbf{k}_c\mathbf{k}_v) - K^d(\mathbf{k}'_c\mathbf{k}'_v,\mathbf{k}_c\mathbf{k}_v), \quad (3.2)$$

with $\delta_S = 0$ for spin triplet states and $\delta_S = 1$ for spin singlet states. The direct interaction kernel K^d for the screened Coulomb potential w is given by the integral

$$\begin{aligned} K^d(\mathbf{k}'_c\mathbf{k}'_v,\mathbf{k}_c\mathbf{k}_v) &= W(\mathbf{k}'_c\mathbf{k}_c,\mathbf{k}'_v\mathbf{k}_v) \\ &= \int d\mathbf{r}'d\mathbf{r}\psi^*_{\mathbf{k}'_c}(\mathbf{r}')\psi_{\mathbf{k}_c}(\mathbf{r}')w(\mathbf{r}',\mathbf{r})\psi_{\mathbf{k}'_v}(\mathbf{r})\psi^*_{\mathbf{k}_v}(\mathbf{r}), \end{aligned} \quad (3.3)$$

and the exchange interaction kernel K^x for the bare Coulomb potential v is

$$K^x(\mathbf{k}'_c\mathbf{k}'_v,\mathbf{k}_c\mathbf{k}_v) = \int d\mathbf{r}'d\mathbf{r}\psi^*_{\mathbf{k}'_c}(\mathbf{r}')\psi_{\mathbf{k}'_v}(\mathbf{r}')v(\mathbf{r}',\mathbf{r})\psi_{\mathbf{k}_c}(\mathbf{r})\psi^*_{\mathbf{k}_v}(\mathbf{r}), \quad (3.4)$$

where ψ is the single particle wave function.

The quasi-particle energies are calculated from the single particle energy $\epsilon_{\rm sp}(\mathbf{k})$ by in-

cluding the self-energy corrections $\Sigma(\mathbf{k})$:

$$E(\mathbf{k}_c) = \epsilon_{\rm sp}(\mathbf{k}_c) + \Sigma(\mathbf{k}_c), \tag{3.5}$$

$$E(\mathbf{k}_v) = \epsilon_{\rm sp}(\mathbf{k}_v) + \Sigma(\mathbf{k}_v), \tag{3.6}$$

where $\Sigma(\mathbf{k})$ is expressed as

$$\Sigma(\mathbf{k}_c) = -\sum_{\mathbf{q}} W[\mathbf{k}_c(\mathbf{k}+\mathbf{q})_v, (\mathbf{k}+\mathbf{q})_v\mathbf{k}_c], \tag{3.7}$$

$$\Sigma(\mathbf{k}_v) = -\sum_{\mathbf{q}} W[\mathbf{k}_v(\mathbf{k}+\mathbf{q})_v, (\mathbf{k}+\mathbf{q})_v\mathbf{k}_v]. \tag{3.8}$$

In order to obtain the kernel and self energy, the single particle Bloch wave function $\psi_{\mathbf{k}}(\mathbf{r})$ here is approximated by an ETB wave function. The dielectric screening effect is considered within a random phase approximation (RPA), in which the static screened Coulomb interaction is given by

$$W = \frac{V}{\kappa\epsilon(\mathbf{q})}, \tag{3.9}$$

with the dielectric function $\epsilon(\mathbf{q}) = 1 + v(\mathbf{q})\Pi(\mathbf{q})$ that describes effects of the polarization of the π bands. The effect of electrons in core states, σ bonds, and the surrounding materials are all represented by a static dielectric constant κ. In the later chapter we will see κ is a very crucial parameter for the environmental effects. By calculating the polarization function $\Pi(\mathbf{q})$ and the Fourier transformation of the unscreened Coulomb potential $v(\mathbf{q})$, the exciton energy calculation can be performed. For 1D materials, the Ohno potential is commonly used for the unscreened Coulomb potential $v(\mathbf{q})$ for π orbitals [9]. After obtaining the excitation energy Ω_n, the exciton binding binding energy $E_{\rm bd}$ can be calculated by substracting the quasi particle energy $E_{\rm QP} = E_c(\mathbf{k}_c) - E_v(\mathbf{k}_v)$ with Ω_1,

$$E_{\rm bd} = E_{\rm QP} + \Omega_1. \tag{3.10}$$

Here Ω_1, which is the first (lowest) exciton state, is interpreted as the transition energy E_{ii},

where an electron and a hole lie on the same i-th cutting line with respect to the K point of the 2D Brillouin zone of graphene. The difference between E_{ii} and the single particle band gap gives the many-body corrections $E_{\rm mb}$ which is also the difference between the self energy and binding energy,

$$E_{\rm mb} = \Sigma - E_{\rm bd}. \tag{3.11}$$

3.2 Exciton symmetry

To discuss the exciton symmetry, wave vectors $\bar{\mathbf{K}}$ for center-of-mass motion and $\mathbf{k}$ for relative motion are introduced,

$$\bar{\mathbf{K}} = (\mathbf{k}_c - \mathbf{k}_v)/2, \quad \mathbf{k} = \mathbf{k}_c + \mathbf{k}_v. \tag{3.12}$$

The exciton state can then be denoted as $|\mathbf{k}, \bar{\mathbf{K}}\rangle$ and the Bethe-Salpeter equation is rewritten in terms of $\bar{\mathbf{K}}$ and $\mathbf{k}$. Because the Coulomb interaction is related to the relative coordinate of an electron and a hole, the excitons in SWNTs can be classified according to the $2\bar{\mathbf{K}}$ value in the regions shown in Fig. 3-1.

Fig. 3-1: fig/fch3-wfzone.pdf

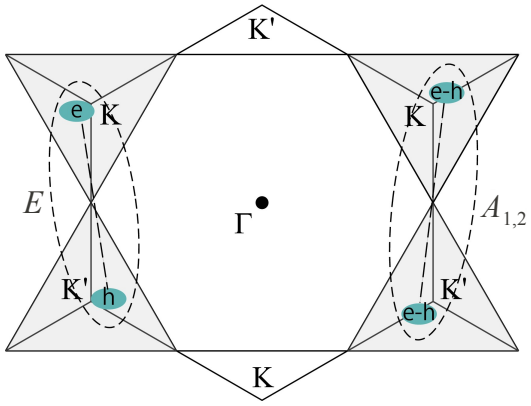

Figure 3-1: Symmetry of an exciton. If both the electron and hole are from the K (or K′) region (right side of the above figure), the corresponding exciton is an $A_{1,2}$ symmetry exciton. If an electron is from the K region and a hole is from the K′ region (left side of the above figure), the corresponding exciton is an E symmetry. One more case is not shown here, the E^* exciton, which is just an opposite situation of the E exciton.

There are three inequivalent regions in the 2D Brillouin zone of graphene, i.e., two triangle regions around K, K′ and a hexagonal region around the Γ point. For SWNTs, the optical transitions are related to the electron and hole on the cutting lines in the K or K′ regions. If both the electron and hole are from the K (or K′) region, the corresponding exciton is an $A_{1,2}$ symmetry exciton. The center-of-mass momentum $2\bar{\mathbf{K}}$ lies in the Γ region and $\mathbf{k}$ will be around K (or K′) region. If an electron is from the K region and a hole is from the K′ region, the corresponding exciton is an E symmetry. The momentum $2\bar{\mathbf{K}}$ lies in the K region. If an electron is from the K′ region and a hole is from the K region, their $2\bar{\mathbf{K}}$ lies in the K′ region, and this exciton is an E symmetry exciton. The E and E^* excitons, which have a large angular momentum for the center-of-mass momentum, are dark excitons because the photon wave vector is nearly zero. For A excitons, the electron-hole pair $|\mathbf{k}_c, \mathbf{k}_v\rangle = |\mathbf{k}, \bar{\mathbf{K}}\rangle$ with the electron and hole from the K region and $|-\mathbf{k}_c, -\mathbf{k}_v\rangle = -|\mathbf{k}, \bar{\mathbf{K}}\rangle$ with the electron and hole from the K′ region have the same value for $\bar{\mathbf{K}}$. Here $|\mathbf{k}, \bar{\mathbf{K}}\rangle$ is antisymmetric, whereas $-|\mathbf{k}, \bar{\mathbf{K}}\rangle$ is symmetric, under the C_2 rotation. The corresponding excitons are labeled A_2 and A_1 excitons, respectively. The optical dipole moment is defined as

$$M \propto \mathbf{P} \cdot \mathbf{D}\langle\Psi|\nabla|\Psi_0\rangle\rangle, \tag{3.13}$$

with $\langle\Psi|$ and $|\Psi_0\rangle$ denoting the excited and ground states, respectively, and $\mathbf{P}$ is the light polarization vector. The ground state $|\Psi_0\rangle$ has an s symmetry and operator ∇ is antisymmetric under the C_2 rotation. In order to get a nonzero M, $|\Psi\rangle$ thus should be antisymmetric, too. Therefore, A_1 excitons are dark excitons, and only A_2 excitons are bright excitons. Hereafter, only the case of bright excitons is considered for interpreting the experimental results because the resonance Raman spectroscopy (RRS) and photoluminiscence (PL) spectra are related to the optical dipole transition of the bright exciton.

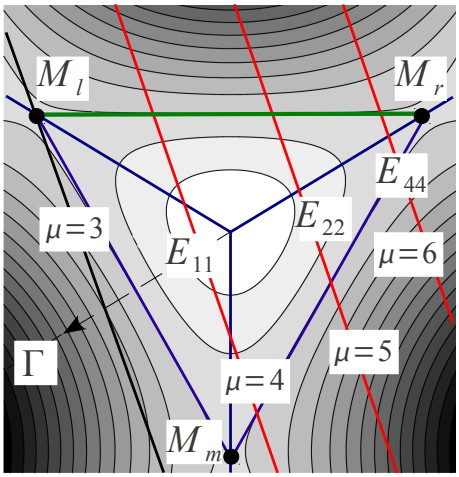

Figure 3-2: Wave vectors of a $(6,1)$ SWNT nanotube around the K point. The cutting lines must cross the $M_l M_r$ line in order to have an E_{ii} within the $3M$ region. The index μ is counted from the Γ point.

3.3 Bright excitons

3.3.1 Condition for the cutting lines

For the bright excitons, the cutting lines k_{ii} near the K point is important to determine exciton energies E_{ii}. A triangular region which connects three M points, i.e., M_l, M_r, and M_m around the K is defined as the 3M triangle as shown in Fig. 3-2. Only in this region the energy dispersion of the conduction (valence) band for a SWNT has a minimum (maximum). The remaining region of the Brillouin zone is a hexagonal region which connects six M points around the Γ point. In the hexagonal region, the conduction (valence) bands have a maximum (minimum). This gives a singular joint of density of states but a minimum electron-photon matrix element at the singular point [41]. Thus a cutting line will not contribute to the optical absorption at E_{ii} if the cutting line lies outside of the $3M$ triangle. As for example, a $(6,1)$ SWNT shown in Fig. 3-2 does not have E_{33} optical absorption because the corresponding cutting line cannot lie within the $3M$ triangle. Therefore, E_{33} is skipped, only E_{11}, E_{22}, and E_{44} are observed in experiments, though all E_{ii} values can be calculated by theory.

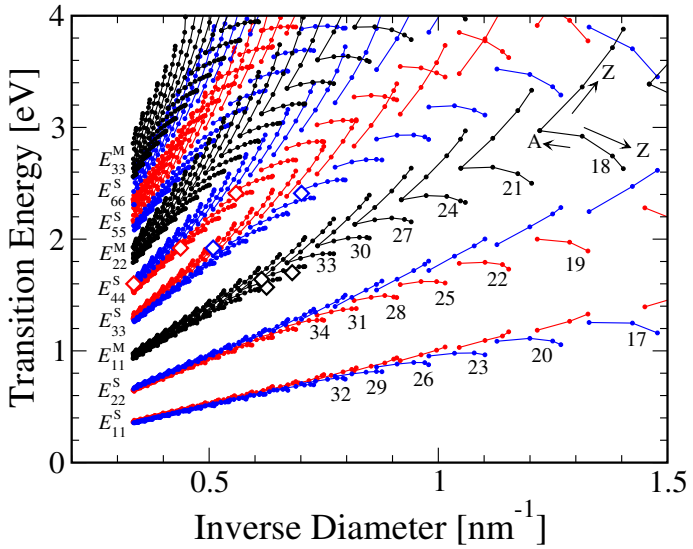

Figure 3-3: The bright exciton energy Kataura plot as a function of inverse diameter $1/d_t$ for $\kappa = 2.22$. The exciton energies E_{ii} shown here are up to E_{66}^{S} and E_{33}^{M}. Black, red, and blue dots correspond to M-, S1-, and S2 SWNTs, respectively. The eight diamond symbols are experimental data by Michel *et al.* (Ref. [42]). The $2n + m$ family patterns are clearly seen for smaller diameter SWNTs. The arrows with A (Z) symbols correspond to the near armchair (zigzag) SWNTs.

3.3.2 Bright exciton energy

Figure 3-3 shows the calculated results for the lowest bright exciton states but different cutting lines k_{ii}, which then give the exciton energies E_{ii}. The results for higher exciton states on a given cutting line is beyond the scope of the present discussion. The Kataura plot in figure 3-3 is given as a function of inverse tube diameter in the range of $0.3 < d_t < 3.0\,\mathrm{nm}$. The E_{ii} calculation is performed by taking a single constant $\kappa = 2.22$ which is fitted from the experimental E_{ii} data of the RRS or PL measurements for SWNT bundle samples. Like the single particle ETB model, the exciton ETB Kataura plot also shows the $2n + m$ family patterns, but unlike the single particle picture this excitonic plot can be adjusted by changing κ.

The eight diamond symbols are experimental results for suspended SWNTs given by

Fig. 3-2: fig/fch3-mmm.pdf
Fig. 3-3: fig/fch3-exkata.pdf

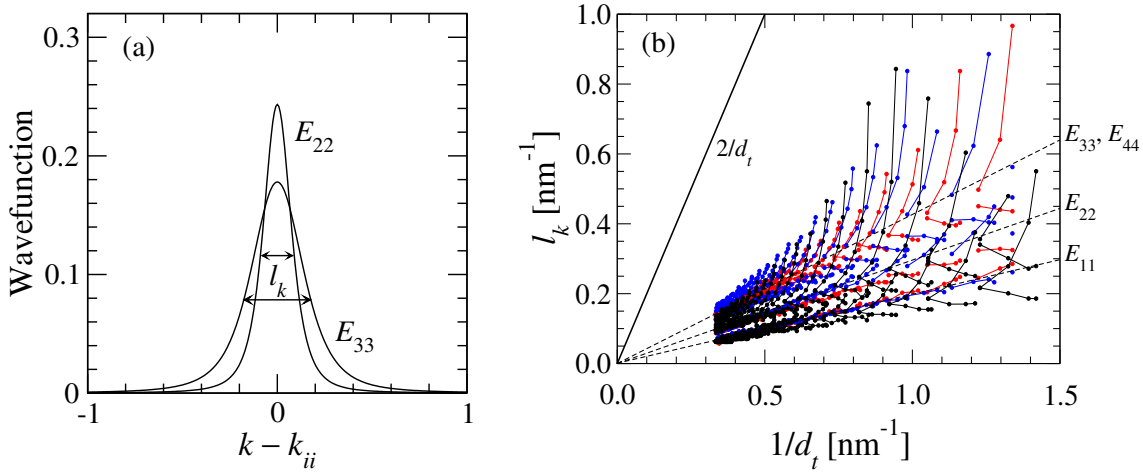

Figure 3-4: (a) Exciton wave functions in 1D k space for a $(20, 0)$ semiconducting SWNT. The states shown here are for E_{22} and E_{33}. The wave function half-width l_k increases with E_{ii}. (b) l_k for many SWNTs as a function of $1/d_t$. The cutting line spacing $2/d_t$ is shown by the solid line for comparison. The dashed lines indicate the corresponding E_{ii} states. The spacing between E_{33} and E_{44} is not distinguished clearly.

Michel *et al.* [42] in which they succeeded with an assignment of (n, m) for SWNTs with diameters of up to 3 nm. Although their results are for isolated suspended SWNTs, and the calculation is for bundles, the calculated results for their assigned (n, m) values reproduce well all eight points within the environmental effect shifts up to 80 meV. This is still much better than another theoretical calculation without the exciton picture which was previously by them to interpret their experimental results because they needed to shift the E_{ii} data by about $0.3 - 0.4$ eV. For a greater accuracy and general understanding of the exciton model, the environmental effect will be discussed in the next chapter, so that a general κ expression is used to construct the Kataura plot.

3.3.3 Exciton size

The localized exciton wavefunction is constructed by mixing many k states in which the mixing coefficients are determined by the BetheSalpeter equation. In Fig. 3-4(a), the wave function for a $(20, 0)$ SWNT is shown. The exciton wave function half-width l_k indicates the

Fig. 3-4: fig/fch3-lk.pdf

exciton size in reciprocal space. Since the Fourier transformation of this wave function will also give a similar localized function, the width in real space gives the exact exciton size or radius, that is the effective distance between an electron and a hole in the bound electron-hole pair. The exciton size in real space is thus inversely proportional to l_k. To study the wave function size dependence on chirality, the width l_k for the E_{11} up to E_{44} states are calculated for all SWNTs with diameters d_t in the same range as in the exciton energy calculation, $0.3 < d_t < 3.0\,\mathrm{nm}$, shown in Fig. 3-4. For comparison, the cutting line spacing $2/d_t$ is also shown in the figure by the solid line. It is clear that l_k is always smaller than the cutting line spacing $2/d_t$. Because l_k measures the extended length of a wave function in k space, this result indicates that one cutting line is sufficient to describe E_{ii} states. The similar family patterns observed in the l_k plot tells us a proportionality between l_k and E_{ii}. Though the proportionality is not direct, but roughly we can say a large l_k means a large E_{ii} or large binding energy E_{bd}, and a small l_k means a small E_{ii} or small E_{bd}.

3.4 Many-body effects

To understand whether the single particle spectra or many-body effects contribute to the large family spread in the exciton Kataura plot, the transition energy E_{11}, the self-energy Σ, the exciton binding energy E_{bd}, and the energy correction to the single particle energy (many-body correction) $\Sigma - E_{\mathrm{bd}}$ are plotted in the same figure (Fig. 3-5). Although both Σ and E_{bd} tend to increase the family spread in smaller diameter SWNTs, the two values almost cancel each other regarding the family spread, leading to a weak chirality dependence. The large family spread observed in E_{ii} is thus concluded to originate from the trigonal warping effect in the single-particle spectra [7]. The net-energy correction (ΣE_{bd}) to the single-particle energy depends predominantly on d_t. The correction has a logarithmic nature, owing to the effect of the Coulomb interaction on the dispersion of graphene [11],

$$E_{\log} = 0.55(2p/3d_t)\log\left[3\left(\frac{3d_t}{2p}\right)\right], \tag{3.14}$$

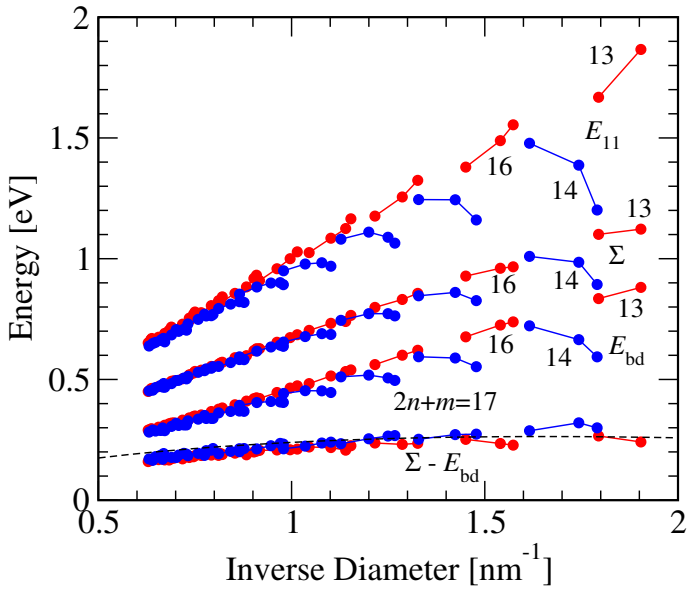

Figure 3-5: The transition energy E_{11}, self energy Σ, binding energy $E_{\rm bd}$, and many-body corrections $\Sigma - E_{\rm bd}$ for the E_{11} states based on the ETB model. The red and blue dots correspond to S1- and S2-SWNTs, respectively. The dashed line is calculated by Eq. 3.14.

where p is an integer corresponds to the ratio of the distances of the cutting lines for each E_{ii} transition from the K-point in 2D Brillouin zone of graphene [7], $p = 1, 2, 3, 4, 5$ stands for $E_{11}^{\rm S}$, $E_{22}^{\rm S}$, $E_{11}^{\rm M}$, $E_{33}^{\rm S}$, and $E_{44}^{\rm S}$, respectively. In Fig. 3-5, $E_{\log}$ with $p = 1$ is plotted as a dashed line. It can be seen that the many-body correction $\Sigma - E_{\rm bd}$ calculated in the exciton picture follows the logarithmic behavior very well.

However, the cancellation of $E_{\rm bd}$ and Σ does not work well for higher E_{ii} values. Araujo *et al.* observed that for $E_{33}^{\rm S}$ and $E_{44}^{\rm S}$ and that a universal curve for the many body correction for $E_{33}^{\rm S}$ and $E_{44}^{\rm S}$ apparently deviates from that for $E_{11}^{\rm S}$ and $E_{22}^{\rm S}$ [26], so they claimed $E_{33}^{\rm S}$ and $E_{44}^{\rm S}$ are not related to the exciton states. Actually this is a wrong conclusion, since the self-energy becomes much larger than the absolute value of the exciton binding energy with increasing i for E_{ii}, therefore the cancellation of the family spread for the many-body effect does not occur anymore for $E_{33}^{\rm S}$ and $E_{44}^{\rm S}$. This means $E_{33}^{\rm S}$ and $E_{44}^{\rm S}$ are nothing but exciton states, too.

Fig. 3-5: fig/fch3-mbe.pdf
Fig. 3-6: fig/fch3-mass.pdf

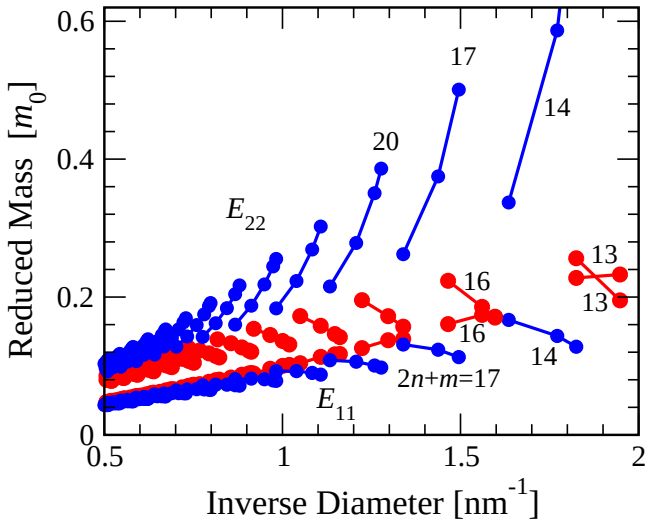

Figure 3-6: The reduced (effective) mass for the first and second transitions for S-SWNTs calculated within the ETB model. The red and blue dots denote S1- and S2-SWNTs, respectively.

Similarity in the family patterns

The family behavior in E_{ii}, $E_{\rm bd}$, and l_k arises from the same reason, that is, from the trigonal warping effect. The first van Hove singularities (VHSs) for S1- and S2 SWNTs are outside (that is, along the KM line), and inside (along the ΓK line) of the first Brillouin zone of graphene. The situation is opposite for the second VHSs. Around the K point, the energy bands of graphene are generally more flat inside the Brillouin zone than outside the Brillouin zone. Thus, the reduced mass $\mu = (1/m_{\rm e}^* + 1/m_{\rm h}^*)^{-1}$ (where $m_{\rm e}^*$ and $m_{\rm h}^*$ are respectively electron and hole effective mass) is generally larger inside and smaller outside the Brillouin zone. In this sense, μ exhibits a tube type dependence as shown in Fig. 3-6. This tube type dependence for μ will bring a similar tube type dependence for l_k and $E_{\rm bd}$. For example, for E_{22} states, μ is larger for S2-SWNTs than that for S1-SWNTs and thus l_k and $E_{\rm bd}$ are longer and larger, respectively. The effective mass also shows family patterns, the similar family patterns appear in l_k and $E_{\rm bd}$.

Chapter 4

The environmental effect

The transition energies E_{ii} are now understood in terms of the bright exciton energy within the extended tight-binding (ETB) calculation which includes curvature optimization [8], and many-body effects [30]. Experimentally, the assignments of E_{ii} for SWNTs over a broad range of diameter ($0.7 < d_t < 3.8\,\mathrm{nm}$) and energy ($1.2 < E_{ii} < 2.7\,\mathrm{eV}$), and also for a variety of surrounding materials are now available [43]. This makes it possible to accurately determine the effect of the general dielectric constant κ on E_{ii}. Here "general" means that a single κ value, e.g., $\kappa = 2.22$ in the previous chapter, is no longer valid because it is still insufficient to solve the environmental effect. Instead, κ is now expressed in a certain functional form. In this chapter, a dielectric constant model is developed in order to reproduce many experimental E_{ii} values for different environmental conditions.

4.1 Energy shift by the environment

In Equation (3.9), κ is introduced to include the screening effect from the environment. Actually it also includes the tube term, but the change of κ for the same tube indicates only the materials surrounding the tube is changed. By studying the exciton energy dependence on κ, we can see how significant is the environmental effect shifts the excitation energy. By changing the κ value from 3 to 2, the exciton energy is calculated and the energy shift

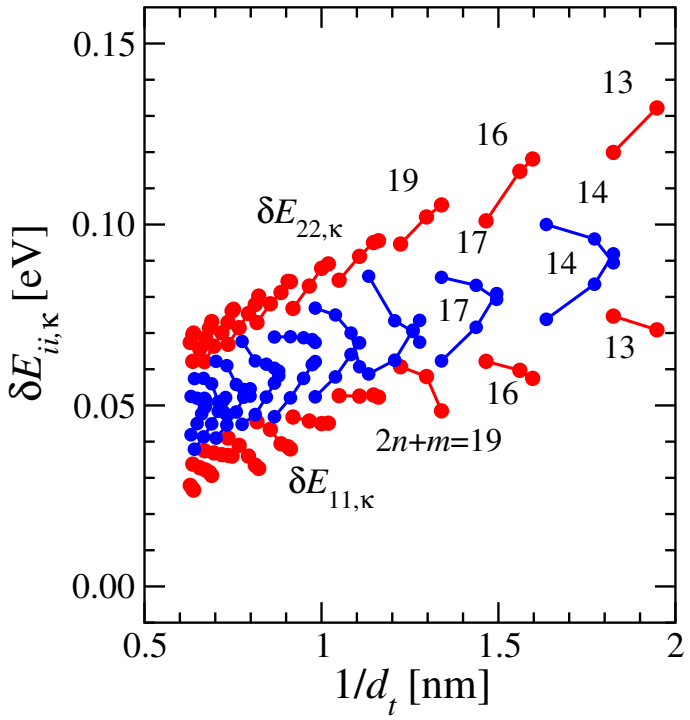

Figure 4-1: The E_{11} and E_{22} transition energy shifts by κ changing from 3 to 2: $\delta E_{ii,\kappa} = E_{ii}(\kappa = 2) - E_{ii}(\kappa = 3)$. Red and blue dots correspond to S1- and S2- SWNTs, respectively.

$\delta E_{ii,\kappa} = E_{ii}(\kappa = 2) - E_{ii}(\kappa = 3)$ is obtained. The results are shown in Fig. 4-1. In the figure, it is clear that there are also tube type and $2n + m$ family dependences for $\delta E_{ii,\kappa}$. Comparing these results with the E_{ii} and l_k patterns in Figs. 3-3 and 3-4, respectively, it is seen that the tube type dependence here is different from that in E_{ii} and l_k. For $\delta E_{11,\kappa}$ within the same $2n + m$ family, the value of $\delta E_{11,\kappa}$ increases with the increase of chiral angle θ for S1-SWNTs, while it decreases with θ for S2-SWNTs. In contrast, for $\delta E_{11,\kappa}$ case, its value decreases with θ for S1-SWNTs and increases with θ for S2-SWNTs. These trends are consistent with the experimental observation by Ohno *et al.* [44].

The excitation energy shifts δE_{ii} are generally up to 80 meV [16, 45], and in some rare cases are up to 100 meV [31]. These facts are in good agreement with the calculation results given in Fig. 4-2, in which the difference between E_{ii} with $\kappa = 1$ and $\kappa = 5$ is about 80 meV. The example nanotube is $(6, 5)$, and the plotted energy dependences are for E_{11} and E_{22}. It

Fig. 4-1: fig/fch4-dex.pdf

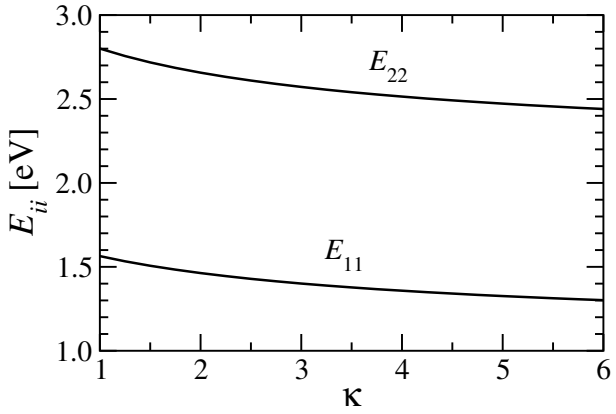

Figure 4-2: Exciton energy E_{ii} versus κ for a $(6,5)$ SWNT.

can be seen that E_{ii} is inversely proportional to κ, approximately. In the experimental point of view, the environmental dielectric constants can be varied with the value from close to 1 up to a large value. When κ is large, for example $\kappa > 5$, the excitation energy will approach the single particle energy.

4.2 Optimized dielectric constant

Fig. 4-2: fig/fch4-kapp.pdf
Fig. 4-3: fig/Fig01.pdf

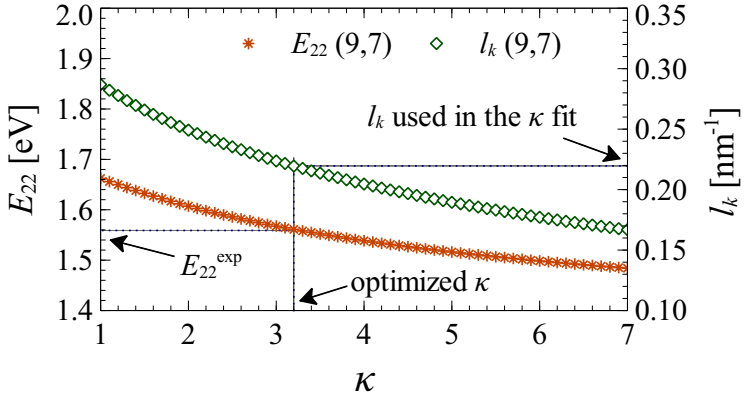

Figure 4-3: Left and right vertical axes show, respectively, the E_{22} and l_k dependences on κ for a (9,7) SWNT. The plot shows how the optimized κ is obtained for a given SWNT in a HiPco sample [16].

Since the use of a single constant κ is not sufficient to accurately reproduce all experimental E_{ii} values [30], we need to adjust the κ value to the experimental E_{ii} value of a given (n, m) SWNT including its environment. To fully account for the observed energy-dependent E_{ii} redshift, the total κ values, $1/\kappa = C_{\rm env}/\kappa_{\rm env} + C_{\rm tube}/\kappa_{\rm tube}$ [18], are fitted to minimize $E_{ii}^{\rm exp} - E_{ii}^{\rm cal}$. In Fig. 4-3, E_{22} versus κ is plotted for a (9,7) SWNT. From the plot, one can get an "optimized" κ which reproduces the experimental E_{22} value ($E_{22}^{\rm exp}$). The plot also gives the related l_k (l_k^{-1}) denoting the respective exciton size value in reciprocal (real) space. Repeating this procedure for many (n, m) and E_{ii} values for several samples, we obtain a set of optimized κ values for the different samples.

4.3 Dielectric constant model

Using the optimized κ values, a general κ function is modeled to have the functional form

$$\kappa \approx C_\kappa \left[p^a (1/d_t)^b (1/l_k)^c \right], \tag{4.1}$$

where the integer p corresponds to the ratio of the distances of the cutting lines for each E_{ii} transition from the K-point in 2D Brillouin zone of graphene [7], and $p = 1, 2, 3, 4, 5$ stands for $E_{11}^{\rm S}$, $E_{22}^{\rm S}$, $E_{11}^{\rm M}$, $E_{33}^{\rm S}$, and $E_{44}^{\rm S}$, respectively. The variable l_k is involved in the κ function because of the screening by the different environments that modify the exciton size. The parameters (a, b, c) that are thus determined are common for all different samples so as to both optimize the correlation between κ and (p, d_t, l_k), and to minimize differences between theory and experiment. The experimental E_{ii} data considered here are based on resonant Raman excitation profiles for the SG [31, 32], ACCVD [26, 32] and HiPco SWNTs wrapped by SDS [16].

In Fig. 4-4, it is shown a series of results for the κ function for different samples. For each sample, the κ functions for the lower transitions ($E_{11}^S, E_{22}^S, E_{11}^M$) and higher transitions (E_{33}^S, E_{44}^S) can be unified, and it is noted that this unity was missing in the previous

Fig. 4-4: fig/Fig02.pdf

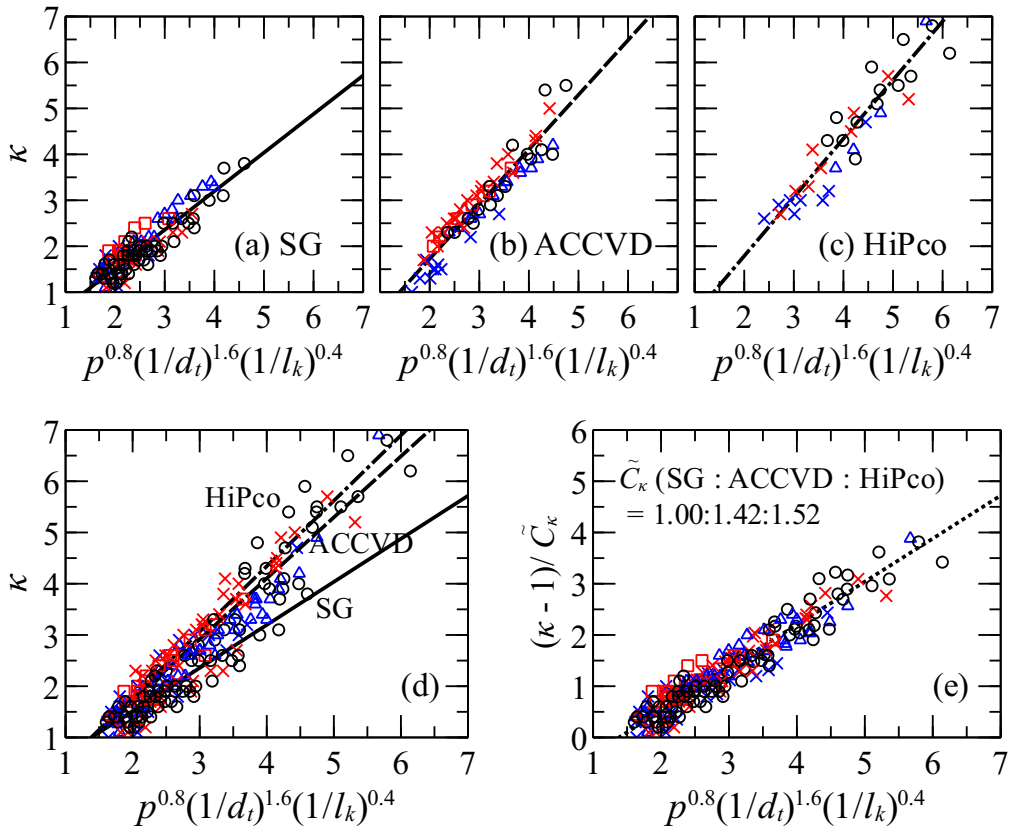

Figure 4-4: The κ function for: (a) SG, (b) ACCVD, and (c) HiPco samples. (d) Data for the three samples are plotted on the same figure with fitted slope C_κ for each sample. (e) All the κ functions collapse on to a single line after dividing each function with the corresponding $\tilde{C}_\kappa$. The following symbols are used: $E_{11}(\circ)$, $E_{22}(\times)$, $E_{33}(\triangle)$, $E_{44}(\square)$. Black, red, and blue colors, respectively, denote M-, S1-, and S2-SWNTs.

work [32]. Considering l_k explicitly in the present work is important to properly describe the environmental effect. Indeed, the exciton size is a key variable in the dielectric screening of excitons. Keeping d_t constant, the κ values for higher E_{ii} are smaller than that for lower E_{ii}. Thus l_k^{-1} (the exciton size in real space) is also smaller because only a small amount of the electric field created by an electron-hole pair will influence the surrounding materials. If l_k for a particular E_{ii} is kept constant, tubes with a smaller d_t will experience a stronger dielectric screening effect because the electric field lines from the electron-hole pair can easily go outside of the tube, thus explaining why both d_t and l_k are taken into account in the κ formulation. The values of (a, b, c) from the best fitting result are found to be (0.80 ± 0.10,

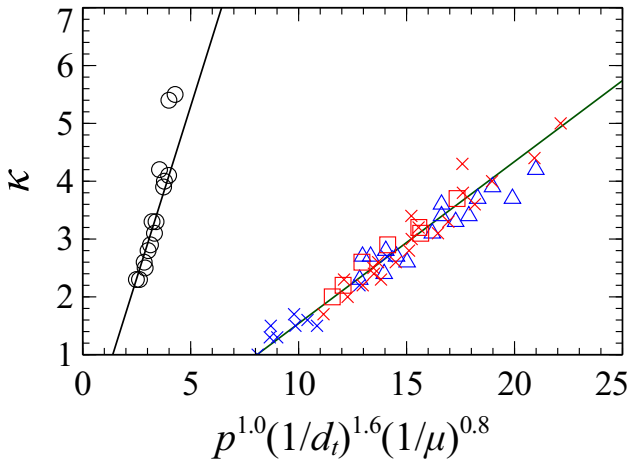

Figure 4-5: κ as a function of (p, d_t, μ). Two different functions are needed, each of which for M- and S-SWNTs, respectively. The data plotted here are based on the ACCVD sample. The following symbols are used: $E_{11}(\circ)$, $E_{22}(\times)$, $E_{33}(\triangle)$, $E_{44}(\square)$. Black, red, and blue colors, respectively, denote M-, S1-, and S2-SWNTs.

$1.60 \pm 0.10,\ 0.40 \pm 0.05$), respectively. This result is somehow indicating another scaling relation of excitons similar to the previously reported scaling law which relates $E_{\rm bd}$ with d_t, κ, and the "effective mass" μ [13]. If we adopt $E_{\rm bd} \propto \mu^{\alpha-1} d_t^{\alpha-2} \kappa^{-\alpha}$ with $\alpha = 1.40$ as is given by Eq. (7) in Ref. [13], we can obtain the form of Eq. (4.1) by making a conversion of variables from $E_{\rm bd}(\mu, d_t, \kappa)$ to $\kappa(p, d_t, l_k)$. It is also found that if we replace l_k in Eq. (4.1) by μ, two scaling relations will be needed, one for M-SWNTs and another for S-SWNTs, as can be seen in Fig. 4-5. This is because $E_{\rm bd}$ for an M-SWNT is screened by free electrons even for a similar μ value for the photo-excited carriers. Using l_k in the κ function thus gives us a unified scaling relation for both M- and S-SWNTs. The scaling law itself originates from the nature of the Coulomb potential that always scales with some size parameters.

Looking carefully at the plots for each sample in Fig. 4-4, the only difference we can find between the various plots is the slope or gradient C_κ of the κ function. Values C_κ for the SG, ACCVD, and HiPco samples are 0.84, 1.19, and 1.28, respectively, where omit the units of C_κ are omitted. We expect that such differences arise from the environmental effects on the exciton energies. Therefore, we can assume each C_κ characterizes the environmental

Fig. 4-5: fig/fch4-wemass.pdf

dielectric constant $\kappa_{\rm env}$ of each sample. The argument is as follows. As discussed in Ref. [18], κ can be modeled in analogy to a series connection of two capacitors, one for the tube ($\kappa_{\rm tube}$) and another one for the environment ($\kappa_{\rm env}$). For a given SWNT, the tube term $\kappa_{\rm tube}$ remains the same and the environment term $\kappa_{\rm env}$ is modified when κ changes. The difference in C_κ must then come from the difference in $\kappa_{\rm env}$. The SG sample has the largest E_{ii} and hence the smallest κ relative to any other samples discussed in the literature [31], so for simplicity we normalize C_κ of the SG sample to be $\tilde{C}_\kappa({\rm SG}) = 1.00$. The values of $\tilde{C}_\kappa$ for the other samples can then be determined by taking the ratio of their C_κ to that for the SG sample. Thus $\tilde{C}_\kappa$ for the SG, ACCVD, and HiPco samples becomes 1.00, 1.42, and 1.52, respectively. If we now plot the ratio $\kappa/\tilde{C}_\kappa$ for each sample, it is found that all points collapse on to a single line, as shown in Fig. 4-4(e). This fact gives further support for the use of $\tilde{C}_\kappa$ as a unique parameter for each environment.

4.4 Energy shift formula

With the knowledge of $\tilde{C}_\kappa$ for several types of environments, we are now ready to use these results in practical applications. To a first approximation, the energy shift $\delta E_{ii}^{\rm env}$ due to different environments (Fig. 4-6) is fitted by

$$\delta E_{ii}^{\rm env} = E_{ii}^{\rm SG} - E_{ii}^{\rm env} \equiv \tilde{C}_\kappa \left[A + B\left(\frac{p}{d_t}\right) + C\left(\frac{p}{d_t}\right)^2 \right], \tag{4.2}$$

where A, B, C, are parameters common to all types of environments and $E_{ii}^{\rm env}$ is calculated with the κ function obtained previously. The best fits for A, B, and C were found to be -42.80 ± 1.26 meV, 46.34 ± 1.32 meV $\cdot$ nm, and -7.47 ± 0.65 meV $\cdot$ nm^2, respectively. The SG sample is then fixed as a standard, and all E_{ii} values for the other environments can be calculated simply by

$$E_{ii}^{\rm env} = E_{ii}^{\rm SG} - \delta E_{ii}^{\rm env}. \tag{4.3}$$

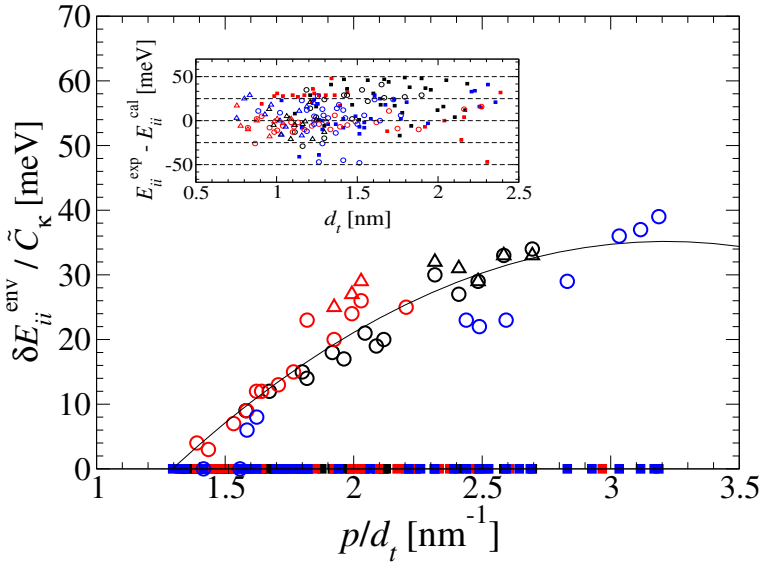

Figure 4-6: $\delta E_{ii}^{\rm env}$ versus d_t, scaled by $\tilde{C}_\kappa$. Circles and triangles, respectively, denote ACCVD and HiPco samples. Many square symbols on the zero line denote the SG sample which is taken as the standard. The inset shows differences between experimental (exp) and calculated (cal) E_{ii} values for all samples, showing good agreement between experiment and our model.

This treatment thus provides a general way to obtain the Kataura plot for SWNTs in any type of environment within an accuracy of 50 meV for all energy regions and d_t as shown in inset of Fig. 4-6).

4.5 Confinement of excitons

In the previous sections, the experimental samples used for the environmental effect analysis were based only on resonance Raman spectroscopy (RRS) data. The same treatment can also be applied for the photoluminiscence (PL) E_{ii} data. However, when we focus our attention to the lowest transitions, E_{11} region, we can find a systematic deviation of the κ values for type-I and type-II S-SWNTs (or also denoted S1- and S2-SWNTs, respectively). It is suggested that the E_{11} energies observed by photoluminescence are upshifted to the calculated E_{11} energies due to the confinement of excitons in the SWNTs. Considering this effect, the

Fig. 4-6: fig/Fig03.pdf

Table 4.1: List of $\tilde{C}_\kappa$ values obtained for different samples.

Measurement	RRS		
Synthesis method (Environment)	SG (as-grown)	ACCVD (as-grown)	HiPco (SDS)
$\tilde{C}_\kappa$	1.00 ± 0.08	1.42 ± 0.03	1.52 ± 0.05
Measurement	PL		
Synthesis method (Environment)	HiPco (SDS)	ACCVD (HEX)	ACCVD (CL)
$\tilde{C}_\kappa$	1.54 ± 0.05	1.77 ± 0.04	2.06 ± 0.06

same energy shift formula for the environmental effect as that for the the RRS, that is Equation 4.2, can be used to reproduce experimental E_{ii} values from PL spectroscopy within a good accuracy, too. For the PL treatment, we can use E_{ii} data from the work by Weisman *et al.* [28] and Ohno *et al.* [45] which give SWNTs under three different environments: (i) HiPco SWNTs dispersed in sodium decodyl sulfate (SDS) aquaeous solution [28], (ii) ACCVD trench-suspended SWNTs immersed in hexane (HEX) [45], and (iii) ACCVD trench-suspended SWNTs immersed in chloroform (CL) [45].

In PL spectra, E_{11} energies are given by the emission spectra, while the other higher E_{ii} energies ($i = 2, 3, 4, \ldots$) are given by the absorption spectra. Since there are no PL spectra for M-SWNTs, only S-SWNTs are considered here. As were obtained previously for the RRS E_{ii} data, in Fig. 4-7 it is now given a series of fitted κ as a function of (p, d_t, l_k) obtained from the PL E_{ii} data. For each sample, all the E_{ii} transitions are unified into a single linear κ function with a slope C_κ as indicated by the violet lines in Fig. 4-7(a)-(c). The normalized slope values $\tilde{C}_\kappa$ are also mentioned in the figure and they are compared to the RRS data as are given in Table 4.1. In particular, since it is known that the $\kappa_{\rm env}$ value for chloform is higher than that for hexane [45], the $\tilde{C}_\kappa$ values obtained for these two samples also follow the same behavior. This fact strengthens the previous assumption that C_κ (or $\tilde{C}_\kappa$) characterizes the environmental dielectric constant of the samples. The physical assumption of $\tilde{C}_\kappa$ can also be justified by dividing κ of each sample with its respective $\tilde{C}_\kappa$

Fig. 4-7: fig/fig1.pdf

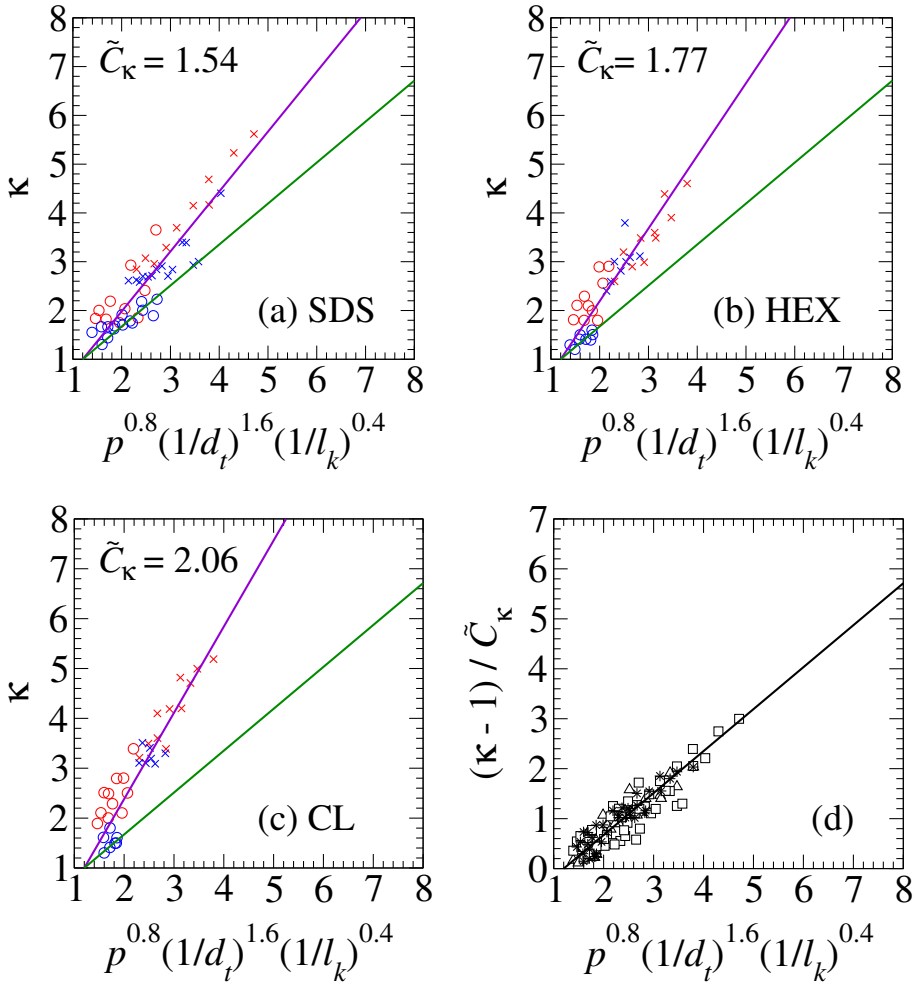

Figure 4-7: The κ function obtained from the PL E_{ii} data. Panel (a) is for the HiPco SWNTs dispersed in SDS aqueous solution. Panels (b) and (c) are for the ACCVD trench-suspended SWNTs immersed in hexane and chloroform, respectively. Circle (cross) symbols are for E_{11} (E_{22}). Red (blue) colors denote S1-(S2-)SWNTs. A green line in each plot is a fitted line for the SG sample as a reference. This line is also a guide for eyes to distinguish the slope for different sample. The effective κ values in (a) are determined from the E_{ii} data in Ref. [28], whereas for those in (b) and (c) are determined from the E_{ii} data in Ref. [45]. Panel (d) shows all κ values from (a)-(c) divided by their corresponding $\tilde{C}_\kappa$. Squares, triangles, and stars are for SDS, HEX, and CL, respectively.

as shown in Fig. 4-7(d), in which all κ data collapse on to a single line. Another point to note is that the $\tilde{C}_\kappa$ values for HiPco SDS samples measured by PL and RRS spectroscopy are similar to each other, indicating the κ model developed in this thesis can be safely used for both PL and RRS. Using Equation 4.2, A, B, C, for the PL data are found to be

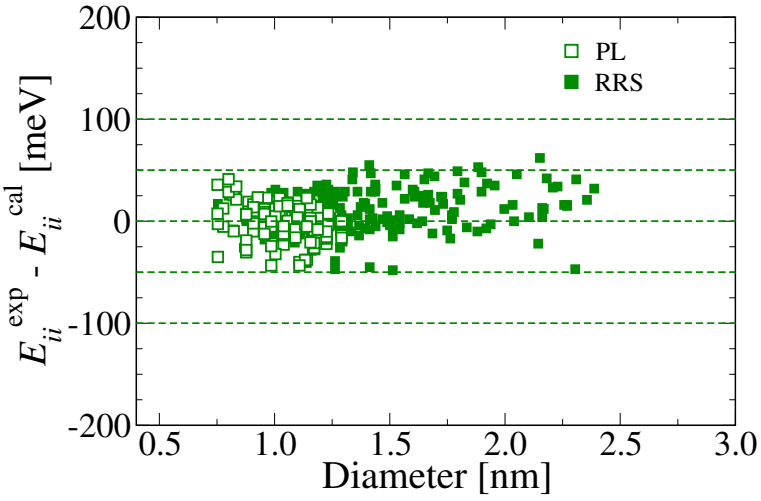

Figure 4-8: Evaluation of the differences between experimental (exp) and calculated (cal) E_{ii} values for all samples, showing good agreement between experiment and our model. Open and filled squares are for PL and RRS data, respectively.

-40.10 ± 1.08 meV, 47.22 ± 1.47 meV $\cdot$ nm, and -6.87 ± 0.36 meV $\cdot$ nm^2, respectively. A good accuracy of $E_{ii}^{\rm exp} - E_{ii}^{\rm cal}$ is obtained again within 50 meV for all energy regions (about $0.9 - 3.0$ eV) and diameter ($0.7 < d_t < 2.5$ nm), as shown in Fig. 4-8.

Unlike the RRS measurements that can give a set of $(E_{11}^{\rm S}, E_{22}^{\rm S}, E_{11}^{\rm M}, E_{33}^{\rm S}, E_{44}^{\rm S})$, the PL data shown in Fig. 4-7 only give $E_{11}^{\rm S}$ and $E_{22}^{\rm S}$, but the number of $E_{11}^{\rm S}$ data observed in PL measurements are much more than those in RRS measurements. We can then analyze the $E_{11}^{\rm S}$ data more carefully. Especially, when we look at the $E_{11}^{\rm S}$ region, denoted by circles in Fig. 4-7, there is a deviated tendency of the κ values for S1- (red circles) and S2- (blue circles) SWNTs. Just to remind, here S1- and S2-SWNTs stand for semiconducting SWNTs with $\mathrm{mod}(2n+m, 3) = 1$ and $\mathrm{mod}(2n+m, 3) = 2$, respectively [7]. For $E_{11}^{\rm S}$, since the S1-SWNTs have larger effective mass than S2-SWNTs [7], we expect a smaller exciton size for S1-SWNTs in real space. This means the S1-SWNTs must have smaller κ values related to the previous explanation about the electric field lines created by excitons. In fact, if the exciton size is small, only small amount of the electric field can be affected by the environment. However, in Fig. 4-7, especially in panels (b) and (c), it is clear that S1-SWNTs tend to have larger

Fig. 4-8: fig/fig2.pdf

κ values compared to S2-SWNTs. This opposite behavior suggests that the exciton might be thermally activated by the center-of-mass motions in a finite SWNT length coupled with phonons, so that the E_{11}^{S} energies obtained from PL measurements are upshifted from the calculated E_{11}^{S} energies. The upshift value should be larger (smaller) for smaller (larger) effective mass, which will be shown as follows.

In the PL process, the excitons are relaxed from the E_{22}^{S} states to the E_{11}^{S} states by the exciton-phonon interaction. This interaction might not perfectly relax the excitons to the lowest exciton states before the electrons and hole recombination gives the emitted light. The exciton state before the recombination is thus slightly upshifted in energy than the real lowest exciton state considered in the calculation because of the quantum confinement of an exciton. This energy difference is denoted by $\Delta E_{11}^{\mathrm{S}}$ that can be understood as the energy upshift of the E_{11}^{S} in the plot of κ.

Since κ is obtained from the experimental E_{11}^{S} energies, the $\Delta E_{11}^{\mathrm{S}}$ values should shift the effective κ depending on the tube type. A good parameter for this situation is the center-of-mass $M_{\mathrm{CM}} = (m_{\mathrm{e}}^{*} + m_{\mathrm{h}}^{*})/2$ (here m_{e}^{*} and m_{h}^{*} are the electron and hole effective masses, respectively), because M_{CM} of a S1-SWNT is generally larger than that of a S2-SWNT for a similar d_t. Then, it is expected that $\Delta E_{11}^{\mathrm{S}} \sim \hbar^2 k_{\mathrm{CM}}/2M_{\mathrm{CM}}$ for the S1-SWNTs should be smaller than that for the S2-SWNTs, so that the κ values for S1-SWNTs will be upshifted smaller. This will result in the correct tendency of the κ values, that is, the κ values for S1-SWNTs are smaller than those for S2-SWNTs, or at least if we cannot make it, the κ values for both S1- and S2-SWNTs are not separated too much.

We can make a model for $\Delta E_{11}^{\mathrm{S}}$ by considering the exciton motion is restricted in a finite length, analogous to the problem of a particle in a box. $\Delta E_{11}^{\mathrm{S}}$ is expressed as

$$\Delta E_{11}^{\mathrm{S}} = \frac{\int_0^\infty E D(E) f(E) \mathrm{d}E}{\int_0^\infty D(E) f(E) \mathrm{d}E}, \tag{4.4}$$

where $D(E)$ is the electronic density of states and $f(E) = \mathrm{e}^{-(E/k_{\mathrm{B}}T)}$ is the phonon distribu-

tion function, $k_{\rm B}$ is the Boltzmann constant, and T is temperature. If we approximate $D(E)$ with the 1D nanotube DOS, $D(E) \propto 1/\sqrt{E}$, it will result in a constant $\Delta E_{11}^{\rm S} = \frac{1}{2}k_{\rm B}T$ at a given temperature, independent of $M_{\rm CM}$, which does not explain the phenomena. Thus we have to model the exciton motion quantum mechanically as a particle in a box which gives discrete energy states E_n as a function of center-of-mass:

$$E_n = \frac{\hbar^2\pi^2}{2M_{\rm CM}L^2}n^2, \tag{4.5}$$

where L is length in which the exciton is confined. The DOS in Equation (4.4) becomes a delta function and thus the integral turns to a summation:

$$\Delta E_{11}^{\rm S} = \frac{\sum_{n=0}^{\infty} E_n {\rm e}^{-(E_n/k_{\rm B}T)}{\rm d}E}{\sum_{n=0}^{\infty} {\rm e}^{-(E_n/k_{\rm B}T)}{\rm d}E}. \tag{4.6}$$

Since E_n is inversely proportional to $M_{\rm CM}$, $\Delta E_{11}^{\rm S}$ is also roughly inversely proportional to $M_{\rm CM}$, as shown by a solid line in Fig. 4-9.

Therefore, we can achieve the expectation to have smaller (larger) $\Delta E_{11}^{\rm S}$ for the S1- (S2-) SWNTs because $M_{\rm CM}$ for the S1- (S2-) SWNTs is larger (smaller). A plot of $\Delta E_{11}^{\rm S}$ calculated from Equation (4-9) for the hexane data is given in Fig. 4-9 with a fixed $L = 20$ nm and $T = 300$ K. The $\Delta E_{11}^{\rm S}$ correction can then be applied to the determination of κ from $E_{11}^{\rm S}$ original data,

$$E_{11}^{\rm S} = E_{11}^{\rm S}({\rm exp}) - \Delta E_{11}^{\rm S}, \tag{4.7}$$

where $E_{11}^{\rm S}$ is now the exciton state free of the center-of-mass motion, that can be used to determine the effective κ.

With the use of $L = 20$ nm, $\Delta E_{11}^{\rm S}$ for S1- and S2-SWNTs are about $20 - 30$ meV and $25-35$ meV, respectively. The corresponding κ upshifts are then about $0.4-0.6$ and $0.5-0.7$

Fig. 4-9: fig/fig3.pdf

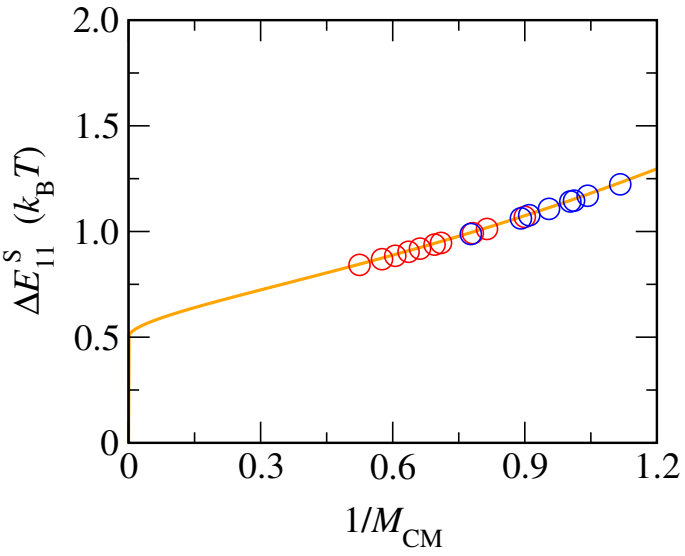

Figure 4-9: $\Delta E_{11}^{\mathrm{S}}$ as a function of M_{CM} for the hexane PL data, where M_{CM} is in the unit of m_0 (electron mass). To get the values shown in the horizontal axis, $1/M_{\mathrm{CM}}$ should be multiplied by a factor $(\hbar^2\pi^2/2m_0L^2)/k_{\mathrm{B}}T$. Red and blue circles denote S1- and S2-SWNTs, respectively. $L = 20$ nm and $T = 300$ K are used in this calculation.

for S1- and S2-SWNTs, respectively. If we use larger L, for example $L = 200$ nm similar to a typical nanotube length found in experiments, $\Delta E_{11}^{\mathrm{S}}$ will be close to a constant $\frac{1}{2}k_{\mathrm{B}}T$. It is concluded that the exciton motions are very restricted in a short finite length L in the center part of the nanotube axis. We do not have a clear image why the exciton is confined in such a short region. A possible explanation is that the exciton is self-trapped by the lattice deformation or defects of a SWNT. These are open issues for the future work.

Chapter 5

Conclusion

In this thesis, it has been shown that the experimental optical transition energies E_{ii} can be reproduced consistently by considering a simple theoretical functional form of the dielectric constant κ, which depends on the nanotube diameter d_t and the exciton size l_k in reciprocal space. It works well for the experimental samples presented here and for the dominant excitonic transitions observed in the experiments: $E_{11}^{\mathrm{S}}, E_{22}^{\mathrm{S}}, E_{11}^{\mathrm{M}}, E_{33}^{\mathrm{S}}$, and E_{44}^{S}.

The functional form of κ is universal so that it can describe a general environmental dielectric screening effect. The results also show a consistent picture for the exciton scaling law in carbon nanotubes. The empirical parameter C_κ (or $\tilde{C}_\kappa$) obtained in this work is found to characterize the environmental effect on E_{ii} in a sense that it specifies the different environments around SWNTs. Using a diameter- and environmental-dependent energy shift formula, many E_{ii} values can be reproduced within an accuracy of 50 meV for SWNTs found in different environments. A careful analysis using the κ function for the photoluminescence E_{ii} data then suggests a confinement effect of excitons in the lowest optical transitions.

Appendix: calculation program

There are several programs used to perform the exciton environmental effects calculation. The main program is to calculate exciton energies for many different dielectric constants κ. This is based on the work by Jiang *et al.* [30] and Sato *et al.* [33]. The results of the program are then stored in a single database file that will be called by other programs for making the κ model and calculating $\delta E_{ii}^{\mathrm{env}}$. All the necessary programs can be found under the following directory in `FLEX` workstation:

`~nugraha/for/enveffect/`

Hereafter, this directory will simply be referred to as `ROOT/` directory. More detail explanations about how to use the programs are given in the `00README` file in each subdirectory of `ROOT`.

Exciton energy

Main program: `ROOT/envkata/envkata.f90`

Database maker: `ROOT/util/makeEii.f90`

Using `envkata.f90`, E_{ii} energies are calculated for all (n, m) SWNTs within $0.5 < d_t < 3.0\,\mathrm{nm}$ and $0 \leq \kappa \leq 8$ for E_{11} up to E_{44}. In a single run of the program, the necessary inputs are only an (n, m) value, an index i of E_{ii}, and a κ value. However, since we want to have a unified database for many parameters, the program is then run many times so that the

desired d_t and κ ranges are satisfied. The diameter range is controlled by variables `dtmin` and `dtmax` in `envkata.f90` for minimum and maximum diameter, respectively. Here we fix `dtmin = 0.5d0` and `dtmax = 3.0d0`. The `envkata.f90` program needs MPI (message passing interface) for parallel computation. The program is then run by some batch files. An example of the batch files is shown below for calculations of E_{11} up to E_{44} for S1-SWNTs (or type-I S-SWNTs).

```
#!/bin/bash
for Eii in 1 2 3 4; do
    for x in 0 2 3 4 5 6 7; do
        for y in 0 1 2 3 4 5 6 7 8 9; do
            mpirun -np 5 ./envkata.out s1 $Eii $x$y
        done
    done
done
echo "finish all"
```

In the above script, S1-SWNTs is denoted by the parameter `s1`, and κ is denoted by `xy`. In this notation, `xy` $= 10$ stands for $\kappa = 1.0$, `xy` $= 20$ stands for $\kappa = 2.0$, and so on. If we want to calculate E_{ii} for M-SWNTs and S2-SWNTs, the parameter `s1` should be replaced by `s0` and `s2`, respectively.

The `makeEii.f90` program is useful for collecting all the separate datafiles resulted by `envkata.f90` into a single database file, namely `eii.dat`. The E_{ii} energies and exciton size l_k are arranged in arrays. The diameters and chiral angles are also stored in this database file. There are two main arrays in that file:

```
Eii(n,m,i,nkappa,flagEii)
dttheta(n,m,flagdt)
```

where `nkappa` is an integer defined by $10(\kappa - 1) + 1$. In the `Eii` array, `flagEii` $= 1$ returns E_{ii}, while `flagEii` $= 2$ returns l_k. In the `dttheta` array, `flagdt` $= 1$ returns d_t, while

`flagEii` = 2 returns θ. So, for example, if we want to get E_{11} for a $(6,5)$ SWNT with $\kappa = 2.2$, we have to give the argument `Eii(6,5,1,13,1)`. The arrays `Eii` and `dttheta` are extensively used in the other programs since we do not have to calculate again `envkata.f90`, so the arrays can save much computational time.

For a given κ, the `envkata.f90` program also gives other constituents of E_{ii}, i.e., single particle energy ($E_{\rm sp}$), exciton binding energy ($E_{\rm bd}$), self energy (Σ), many-body energy ($E_{\rm mb} = \Sigma - E_{\rm bd}$), so that E_{ii} is given by $E_{ii} = E_{\rm sp} + E_{\rm mb}$. An example of the outputs is given here only for a single dielectric constant value, $\kappa = 2.2$, and a subband $i = 1$ (hence E_{11}) for S1-SWNTs. This output is a small part of the larger database file.

n	m	d_t (nm)	θ (rad)	E_{11} (eV)	ϵ (eV)	Σ (eV)	$E_{\rm bd}$ (eV)	$E_{\rm mb}$ (eV)
6	1	0.5252	0.1325	1.8666	2.7476	1.1223	0.8810	0.2413
6	4	0.6893	0.4086	1.3792	2.0554	0.9281	0.6762	0.2518
7	2	0.6492	0.2132	1.4886	2.2139	0.9602	0.7253	0.2349
7	5	0.8226	0.4277	1.1762	1.7379	0.7986	0.5618	0.2368
8	0	0.6356	0.0000	1.5544	2.2928	0.9665	0.7385	0.2281
8	3	0.7773	0.2669	1.2556	1.8559	0.8314	0.6003	0.2310
8	6	0.9564	0.4413	1.0250	1.5078	0.7033	0.4827	0.2205
⋮	⋮	⋮	⋮	⋮	⋮	⋮	⋮	⋮

Example of the output format from the exciton energy program.
Only the case of $\kappa = 2.2$ is given here.

Optimized κ

Main program: `ROOT/diel/calkapp.f90`

The optimized κ values are obtained by matching E_{ii} for a given (n,m) SWNT and subband i from experiments with the E_{ii} calculation database. Because it is not possible to exactly have $E_{ii}^{\rm exp} = E_{ii}^{\rm cal}$, we search for the optimized κ that gives the smallest difference between $E_{ii}^{\rm exp}$ and $E_{ii}^{\rm cal}$. The important parameters to be saved are n, m, p, i, E_{ii}, and corresponding optimized κ. The program needs to call the `Eii` and `dttheta` arrays created by the previous `makeEii.f90` program. Since we only have κ step in the database equal to 0.1 (or one decimal point), we increase the accuracy for finding an optimized κ between two κ points

by interpolating the corresponding E_{ii} values, so that the output for the optimized κ will return the value up to four decimal points. In the input of the program, we give a set of (n, m) values, experimental E_{ii} values, p (cutting line index), and i (subband index). In the following example, some lines of the input for the alcohol-assisted CVD sample are shown.

```
#Alcohol-assisted cvd
 10  7  2.050  3  1
 11  0  1.560  2  2
 20  0  1.924  5  4
 17  1  2.292  4  3
```

Linear regression of κ

Main program: `ROOT/diel/linkapp.f90`

The optimized κ obtained previously are then modeled to satisfy a functional form:

$$\kappa = C_\kappa \left[p^a \left(\frac{1}{d_t}\right)^b \left(\frac{1}{l_k}\right)^c \right] + C_x$$

For a particular sample, we can find the best fit for (a, b, c), C_κ and C_x of that equation by the *least square* method. The result is then coupled to other experimental samples for checking that the same (a, b, c) can be used. After finding the best (a, b, c) values, which are found to be $(a, b, c) = (0.80 \pm 0.10,\ 1.60 \pm 0.10,\ 0.40 \pm 0.05)$, the value of C_κ for each sample is recalculated by fixing a common C_x value for all samples that determines the crossing point between different fitting lines. In this calculation, we have to make sure that the difference between experimental and calculated E_{ii} by κ should be minimum. Also, the correlation coefficient R^2 of the linear regression should be maximum. By these treatments, the κ values for $(E_{11}^{\rm S},\ E_{22}^{\rm S},\ E_{11}^{\rm M},\ E_{33}^{\rm S},\ E_{44}^{\rm S})$ in every experimental sample can be fitted to a single κ function line, and only the C_κ values are different from sample to sample. Using the `linkapp.f90` program, we can then know the C_κ value of a particular input file such

like shown in the previous section for the optimized κ calculation. The normalized C_κ, that is $\tilde{C}_\kappa$, is obtained by dividing the C_κ of a given sample with that of the super-growth (SG) sample.

Energy shift ($\delta E_{ii}^{\rm env}$)

Main program: `ROOT/diel/eshift.f90`

The environmental energy shift is expressed as in Eq. (4.2):

$$\delta E_{ii}^{\rm env} = E_{ii}^{\rm SG} - E_{ii}^{\rm env} \equiv \tilde{C}_\kappa \left[A + B\left(\frac{p}{d_t}\right) + C\left(\frac{p}{d_t}\right)^2 \right].$$

Coefficients A, B, and C can be found by the so-called multiple linear regression method. The above equation can be rearranged to:

$$\frac{\delta E_{ii}^{\rm env}}{\tilde{C}_\kappa} = A + B\left(\frac{p}{d_t}\right) + C\left(\frac{p}{d_t}\right)^2,$$

or we can expressed it as

$$Y = \beta_1 X_1 + \beta_2 X_2 + \beta_3 X_3,$$

where $X_1 = 1$, $X_2 = p/d_t$ and $X_3 = (p/d_t)^2$ are three independent variables in the fitting; and $\beta_1 = A$, $\beta_2 = B$, and $\beta_3 = C$ are constants as the regression coefficients. In the matrix notation, if we have n data of $\delta E_{ii}^{\rm env}$ in a particular sample, we can write $\mathbf{Y} = \mathbf{X}\beta$, where:

$$\mathbf{Y} = \begin{bmatrix} y_1 \\ y_2 \\ \vdots \\ y_n \end{bmatrix}; \quad \mathbf{X} = \begin{bmatrix} x_{11} & x_{12} & x_{13} \\ x_{21} & x_{22} & x_{23} \\ \vdots & \vdots & \vdots \\ x_{n1} & x_{n2} & x_{n3} \end{bmatrix}; \quad \hat{\beta} = \begin{bmatrix} \beta_1 \\ \beta_2 \\ \beta_3 \end{bmatrix}.$$

The coefficients A, B, and C can then be determined by evaluating

$$\hat{\beta} = (\mathbf{X}^T\mathbf{X})^{-1}\mathbf{X}^T\mathbf{Y}.$$

Bibliography

[1] S. Iijima, Nature **354**, 56 (1991).

[2] S. Iijima and T. Ichihashi, Nature **363**, 603 (1993).

[3] R. Saito, M. Fujita, G. Dresselhaus, and M. S. Dresselhaus, Appl. Phys. Lett. **60**, 2204 (1992).

[4] R. Saito, G. Dresselhaus, and M. S. Dresselhaus, *Physical Properties of Carbon Nanotubes*, Imperial College Press, London, 1998.

[5] P. Avouris, Physics Today **62**, 34 (2009).

[6] H. Kataura et al., Synthetic Metals **103**, 2555 (1999).

[7] R. Saito, G. Dresselhaus, and M. S. Dresselhaus, Phys. Rev. B **61**, 2981 (2000).

[8] G. G. Samsonidze et al., Appl. Phys. Lett. **85**, 5703 (2004).

[9] T. Ando, J. Phys. Soc. Jpn. **66**, 1066 (1997).

[10] F. Wang, G. Dukovic, L. E. Brus, and T. F. Heinz, Science **308**, 838 (2005).

[11] C. L. Kane and E. J. Mele, Phys. Rev. Lett. **90**, 207401 (2003).

[12] C. D. Spataru, S. Ismail-Beigi, L. X. Benedict, and S. G. Louie, Phys. Rev. Lett. **92**, 077402 (2004).

[13] V. Perebeinos, J. Tersoff, and P. Avouris, Phys. Rev. Lett. **92**, 257402 (2004).

[14] T. G. Pedersen, Phys. Rev. B **67**, 073401 (2003).

[15] H. Zhao and S. Mazumdar, Phys. Rev. Lett. **93**, 157402 (2004).

[16] C. Fantini et al., Phys. Rev. Lett. **93**, 147406 (2004).

[17] P. T. Araujo, C. Fantini, M. M. Lucchese, M. S. Dresselhaus, and A. Jorio, Appl. Phys. Lett. **95**, 261902 (2010).

[18] Y. Miyauchi et al., Chem. Phys. Lett. **442**, 394 (2007).

[19] T. W. Ebbesen and P. M. Ajayan, Nature **358**, 220 (1992).

[20] T. Guo et al., J. Phys. Chem. **99**, 10694 (1995).

[21] T. Guo, P. Nikolaev, A. Thess, D. Colbert, and R. Smalley, Chem. Phys. Lett. **243**, 49 (1995).

[22] M. Jose-Yacaman, M. Miki-Yoshida, L. Rendon, and J. G. Santiesteban, Appl. Phys. Lett. **62**, 657 (1993).

[23] S. Maruyama, R. Kojima, Y. Miyauchi, S. Chiashi, and M. Kohno, Chem. Phys. Lett. **360**, 229 (2002).

[24] P. Nikolaev et al., Chem. Phys. Lett. **313**, 91 (1999).

[25] Y. Miyauchi, S. Chiashi, Y. Murakami, Y. Hayashida, and S. Maruyama, Chem. Phys. Lett. **387**, 198 (2004).

[26] P. T. Araujo et al., Phys. Rev. Lett. **98**, 067401 (2007).

[27] A. Jorio et al., Phys. Rev. Lett. **86**, 1118 (2001).

[28] R. B. Weisman and S. M. Bachilo, Nano Lett. **3**, 1235 (2003).

[29] M. J. O'Connell et al., Science **297**, 593 (2002).

[30] J. Jiang et al., Phys. Rev. B **75**, 035407 (2007).

[31] P. T. Araujo and A. Jorio, Phys. Status Solidi B **245**, 2201 (2008).

[32] P. T. Araujo, A. Jorio, M. S. Dresselhaus, K. Sato, and R. Saito, Phys. Rev. Lett. **103**, 146802 (2009).

[33] K. Sato, R. Saito, J. Jiang, G. Dresselhaus, and M. S. Dresselhaus, Phys. Rev. B **76**, 195446 (2007).

[34] V. M. Adamyan, O. A. Smyrnov, and S. V. Tishchenko, J. Phys: Conf. Series **129**, 012012 (2008).

[35] T. Ando, J. Phys. Soc. Jpn. **79**, 024706 (2010).

[36] S. M. Bachilo et al., Science **298**, 2361 (2002).

[37] A. Jorio et al., Phys. Rev. Lett. **90**, 107403 (2003).

[38] D. Porezag, T. Frauenheim, T. Köhler, G. Seifert, and R. Kaschner, Phys. Rev. B **51**, 12947 (1995).

[39] E. E. Salpeter and H. A. Bethe, Phys. Rev. **84**, 1232 (1951).

[40] M. Rohlfing and S. G. Louie, Phys. Rev. B **62**, 4927 (2000).

[41] J. Jiang, R. Saito, A. Grüneis, G. Dresselhaus, and M. S. Dresselhaus, Carbon **42**, 3169 (2004).

[42] T. Michel et al., Phys. Rev. B **75**, 155432 (2007).

[43] A. Jorio, M. S. Dresselhaus, and G. Dresselhaus, *Carbon Nanotubes: Advanced Topics in Synthesis, Structure, Properties, and Applications*, Springer-Verlag, Berlin, 2008.

[44] Y. Ohno et al., Phys. Rev. B **73**, 235427 (2006).

[45] Y. Ohno et al., Phys. Status Solidi B **244**, 4002 (2007).

Publication list

Papers

1. A. R. T. Nugraha, R. Saito, K. Sato, P. T. Araujo, A. Jorio, M. S. Dresselhaus: Dielectric constant model for environmental effects on the exciton energies of single wall carbon nanotubes, to appear in Applied Physics Letters vol. 97, issue 9 (2010).

2. A. R. T. Nugraha, K. Sato, and R. Saito: Confinement of excitons for the lowest optical transition energies of single wall carbon nanotubes, submitted to e-Journal of Surface Science and Nanotechnology (2010).

3. P. T. Araujo, A. R. T. Nugraha, K. Sato, M. S. Dresselhaus, R. Saito, and A. Jorio: Chirality dependence of the dielectric constant for the excitonic transition energy of single wall carbon nanotubes, accepted for publication in Physica Status Solidi(b) (2010).

4. K. Sato, R. Saito, A. R. T. Nugraha, and S. Maruyama, Excitonic effects on radial breathing mode intensity of single wall carbon nanotubes, to appear in Chemical Physics Letters (2010), doi:10.1016/j.cplett.2010.07.099.

5. K. Sato, A. R. T. Nugraha, and R. Saito, Excitonic effects on Raman intensity of single wall carbon nanotubes, submitted to e-Journal of Surface Science and Nanotechnology (2010).

Conferences

Poster presentations

1. A. R. T. Nugraha, K. Sato, R. Saito: Simple dielectric constant model for environment effects on exciton energies of single wall carbon nanotubes. Presented in the 38th Fullerene-Nanotubes General Symposium (March 2010), Nagoya, Japan.

2. A. R. T. Nugraha, R. Saito, K. Sato, P. T. Araujo, A. Jorio, M. S. Dresselhaus: Exciton environmental effect in optical transition energies of single-wall carbon nanotubes. Presented in the 37th Fullerene-Nanotubes General Symposium (September 2009), Tsukuba, Japan.

Oral presentations

1. A. R. T. Nugraha, K. Sato, R. Saito: Exciton environmental effects of single wall carbon nanotubes. Presented in the A3 Foresight International Symposium (July 2010), Tokyo, Japan.

2. A. R. T. Nugraha, K. Sato, R. Saito: How could we theoretically treat environment effects on exciton energy calculation of single wall carbon nanotubes? Presented in ATI 2009 Zao Meeting (August 2009), Yamagata-Zao, Japan.